Developing an *in vitro* model and quantitation method for bone marrow adiposity research

Vincensa Nicko Widjaja

Master's Thesis
Åbo Akademi University
28.04.2021

Master's degree in Biomedical Imaging
Specialisation theme: Bone and energy metabolism

Credits: 40 ECTS
Supervisor:
Adj. Prof. Kaisa Ivaska

Passed:
Grade:

Abstract

University of Turku
Faculty of Medicine, Institute of Biomedicine

Vincensa Nicko Widjaja:

Developing an *in vitro* model and quantitation method for bone marrow adiposity research

Master's thesis, 52 pp., 5 appendices
Bone and energy metabolism
April 2021

Bone marrow adipocytes (BMAds) have long been considered a passive and pathological filler within the bone marrow (BM) microenvironment. Recent studies suggest that BMAds may actively influence bone and energy metabolism. As an emerging field, studies to address this discrepancy are hindered by methodological limitations, such as the lack of *in vitro* models and subjectivity in reporting BM adiposity. To that end, we developed a simple adipocyte differentiation model *in vitro* by exposing bone marrow stromal cells (BMSCs) to 10 µg/mL insulin- and 10^{-6} M dexamethasone-containing medium. Adipogenesis was confirmed by the temporal increase in adipocyte-specific mRNA expression and typical morphology of adipocytes with intracellular lipid formation *in vitro*. Using a colour-based segmentation, we developed two image analysis workflows to report area-based adiposity (9.7%) and the proportion of adipocytes obtained by differentiation (13.2%) from our *in vitro* model. To quantitate and analyse BMAds from histological bone sections, we developed a semi-automated quantitation workflow. The algorithm is able to minimise false-positive detections from the area resembling BMAds, such as blood vessels and empty spaces. Our quantitation method is comparable to the manual approach (r^2= 0.92; p< 0.0001), with an average of 17% error detection rate, especially resulting from fused and object-overlapped adipocytes *ex vivo*. The preservation of BMAd morphology during sample processing may improve the accuracy of the quantitation method. From a 16-week old Sprague-Dawley rat, the median size of BMAds *in vivo* was 535.2 (361.4 – 792.3) μm^2. In the future, advancements from the *in vitro* model and quantitation methods would prospectively direct the establishment towards methodological standard in BM adiposity research.

Keywords: *Bone marrow adipocytes, bone and energy metabolism, gene expression, image analysis*

LIST OF ABBREVIATIONS

ACTB	=	beta-actin
Ad.Ar	=	Area of adipocyte
ADIPOQ	=	Adiponectin
BM	=	Bone marrow
BMAd	=	Bone marrow adipocyte
BMP	=	Bone morphogenic protein
BMSC	=	Bone marrow stromal cell
cAMP	=	Cyclic 3',5'-adenosine monophosphate
CD	=	Cluster of differentiation
CEBPA	=	CCAAT Enhancer binding-protein alpha
cMAT	=	Consitutive marrow adipose tissue
CYCB	=	Cyclophilin B
DMSO	=	Dimethyl sulfoxide
FABP4	=	Fatty acid binding protein-4
GLUT4	=	Glucose transporter-4
H.Ar	=	Haematoxylin-stained area
HE	=	Haematoxylin and eosin
HSC	=	Haematopoietic stem cell
IBMX	=	3-isobutyl-1-methylxanthine
IR	=	Insulin receptor
Ma.Ar	=	Marrow area
mRNA	=	messenger ribonucleic acid
mTORC1	=	Mammalian target of rapamycin complex 1
N.Ad	=	Number of adipocytes
ORO	=	Oil-red-O
ORO.Ar	=	Oil-red-O stained area
PPARG	=	Peroxisome proliferated-activated receptor γ
RANKL	=	Receptor activator of nuclear factor κ B ligand
rMAT	=	Regulated marrow adipose tissue
RTqPCR	=	Reverse-transcribed quantitative polymerase chain reaction
SD	=	Sprague-Dawley
UCP1	=	Uncoupling protein-1

TABLE OF CONTENTS

CHAPTER I

REVIEW OF THE LITERATURE

1.1 Bone marrow microenvironment

The dynamics of bone as an organ are orchestrated in synergy from all bone cells, including the bone-building osteoblasts, bone-resorbing osteoclasts, osteocytes, chondrocytes and the haematopoietic cells. The bone marrow (BM) compartment houses two principal stem cell populations to give rise to these cells, classically known as the bone marrow stromal cells (BMSCs), capable of differentiating into either osteoblast or bone marrow adipocyte (BMAd), among others, and haematopoietic stem cells (HSCs) that differentiate into haematopoietic cells or osteoclasts (Calvi, 2020) (**Fig. 1**). Together, osteoblasts and osteoclasts are the key players that are constantly shaping bone structure, a lifelong process known as bone remodelling (Kenkre and Bassett, 2018). Based on this notion, any imbalances that affect one of the cells have considerable consequences to the skeletal health. Based on the tridirectional potential of BMSC differentiation, the skeletal consequences of adipogenesis over osteoblastogenesis have recently gained interest (Ambrosi et al., 2017).

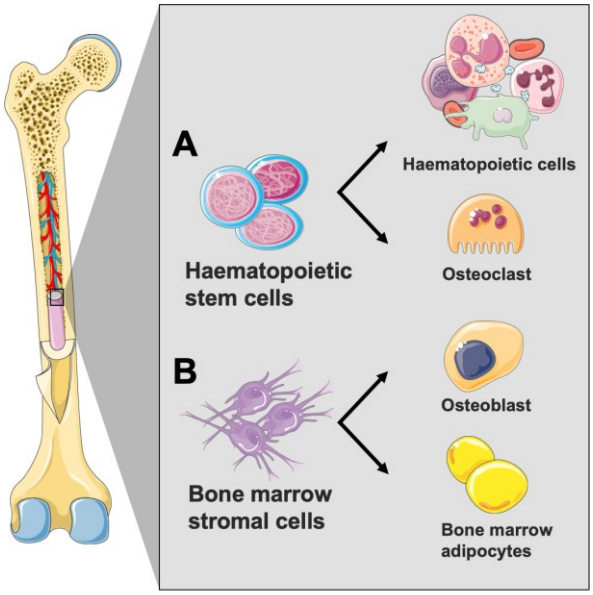

Figure 1. Key players in the bone marrow microenvironment. A simplified view of differentiation potential of **(A)** haematopoietic stem cells and **(B)** bone marrow stromal cells. BMSCs may also differentiate into chondrocytes (not shown). The illustration was created with Servier Medical Art (Servier, France).

1.2 The origin and development of bone marrow adipocytes

Although the classic understanding of BMSC as a source of BM adipogenesis has been well disseminated, specific populations of BMSC have low or high adipogenic potential. Human, mouse and rat BMSC is often defined through the expression of cell surface markers known as cluster of differentiation (CD), such as CD29, CD44 and CD90, among others, and being devoid of HSC surface markers CD34, CD45, and human leukocyte antigen (Boxall and Jones, 2012). At least in mouse, further sorting of BMSC population revealed that the $Sca1^{+}$ $CD24^{-}$ population is highly adipogenic. Contrastingly, the $Sca1^{-}$ population, regardless of CD24 expression, is rather non-adipogenic (Ambrosi et al., 2017). Therefore, the sorting of BMSCs based on surface markers for adipogenic potential is one of the key approaches in delineating the precursor of BMAd *in vivo*.

Upon local and systemic exposure of biochemical (endocrine and paracrine factors) and biophysical (oxidative stress and immobility) factors, adipocyte-specific genes are upregulated through multiple mechanisms depending on the activator element to induce adipogenesis from BMSC (Chen et al., 2016; Hardouin et al., 2016). This first wave of activation induces the expression of the classic pre-adipocyte marker peroxisome proliferated-activated receptor gamma (PPARG) or CCAAT enhancer binding-protein alpha (CEBPA) mainly through the bone morphogenetic protein (BMP) and cytosolic cyclic 3',5'- adenosine monophosphate (cAMP) signalling pathway (Lefterova et al., 2014). Further, these transcription factors promote the expression of adipocyte-specific and non-specific genes to facilitate the phenotype transition from BMSC to mature BMAd, including fatty acid synthase, fatty acid binding protein-4 (FABP4), insulin receptor (IR), glucose transporter-4 (GLUT4) and adipokines leptin and adiponectin (ADIPOQ) (Tang and Lane, 2012). Although known mechanisms are often drug-induced, the physiological signalling map *in vivo* describing BM adipogenesis remains poorly understood.

In 3D bone microenvironment, BMAds exist in a spatiotemporal regulation *in vivo*. The term constitutive and regulated marrow adipose tissue (cMAT and rMAT, respectively) was first coined by Scheller and colleagues (2015) to distinctly classify BMAds based on their characteristics in rodents as shown in **Figure 2A**. They found that cMAT is the first adipose depot to emerge within the skeleton with large and metabolically inert adipocytes

located at the distal end of the bones. Contrastingly, rMAT is rather dispersed within the marrow with smaller cell size and actively interacting with other cells. It was later hypothesised that rMAT, which developed much later in life, might be the active player in regulating bone and energy metabolism.

Following a complete transition from BMSC *in vivo*, BMAd resembles white adipocyte in morphology: a circular cell with prominent singular lipid droplet and cytoplasm enclosing the cell (**Figure 2B**). Unlike white adipocytes, BMAd remains metabolically inert and resists lipolysis (Li et al., 2019). Further, BMAd *in vivo* does not resemble brown adipocytes in morphology nor express uncoupling protein-1 (UCP1), a thermogenic hallmark of brown adipocytes (Craft et al., 2019). At this stage, mature BMAds actively secrete factors that may influence other cells. Most notably, the secretion of leptin, a ligand to the leptin receptor expressed by BMSC, is able to induce further adipogenesis (Yue et al., 2016). Also, it has recently been discovered that adipocytes derived from BMSCs *in vitro* secrete extracellular vesicles containing anti-osteoblastic transcripts to osteoblast, subsequently reducing osteoblast-specific gene expression (Martin et al., 2015). This may provide a mechanistic link to which adipocytes interact with other cells and may be affecting their expression profile.

The mode by which adipogenesis is induced *in vitro* follows the classical notion to upregulate adipocyte-specific gene inducers PPARG and CEBPA. This can be achieved by exposing BMSCs to insulin, dexamethasone and 3-isobutyl-1-methylxanthine (IBMX), among others (Scott et al., 2011; Tratwal et al., 2020b). Insulin promotes mammalian target of rapamycin complex 1 (mTORC1) signalling pathway by activating phosphokinase-B, which in turn induces PPARG expression (Blagosklonny et al., 2009). Dexamethasone raises adipocyte regulator CEBPA while IBMX inhibits phosphodiesterase. In turn, these conditions increase intracellular cAMP level that maintains phosphokinase-A signalling, ultimately induces PPARG expression (Li et al., 2013; Yang et al., 2008). Alternatively, a synthetic PPARG agonist rosiglitazone can be used to potently induce adipogenesis, although its effect may differ from physiological response (Rzonca et al., 2004). **Figure 2C** summarises the mode by which these added compounds induces adipogenesis *in vitro*.

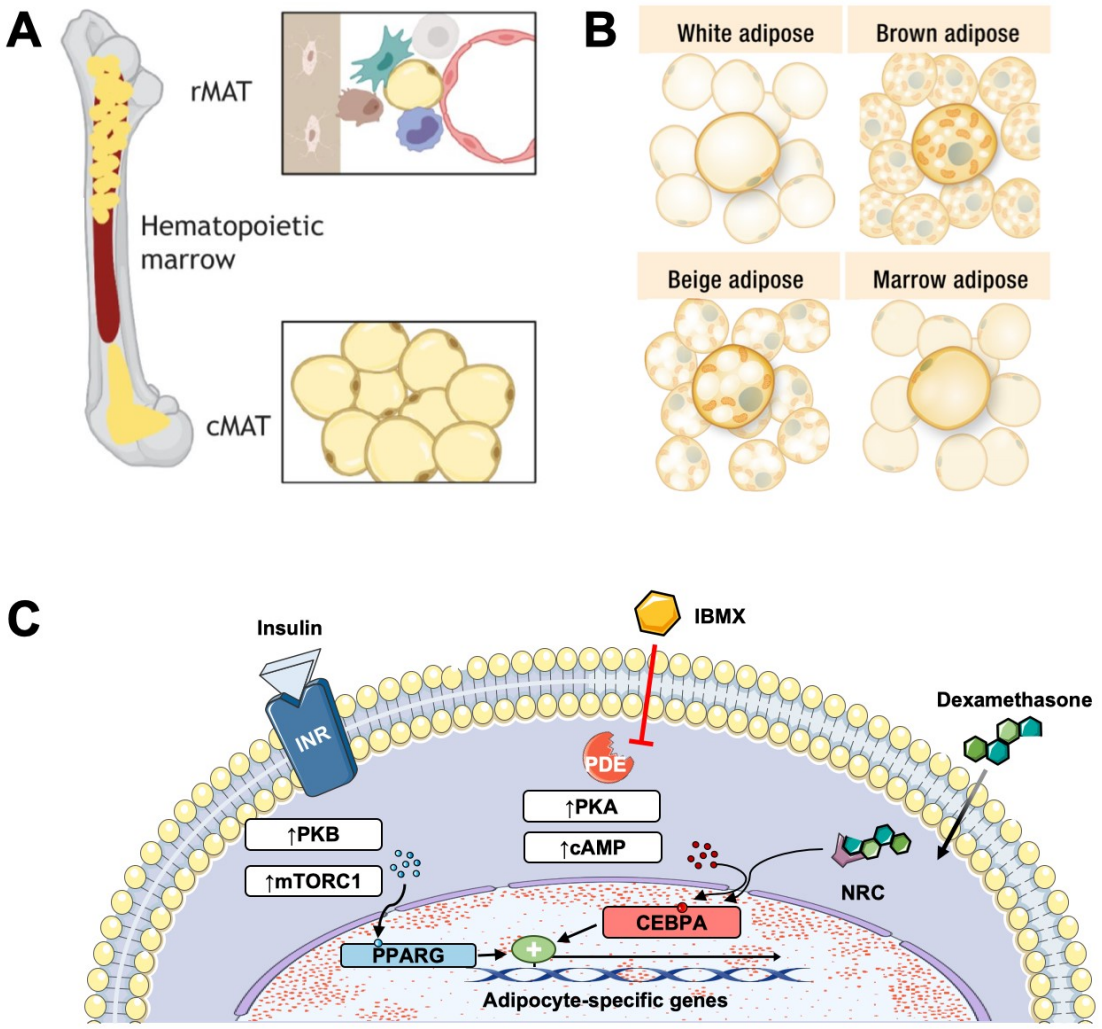

Figure 2. Characteristics of bone marrow adipocytes. (A) Spatiotemporal regulation of marrow adipogenesis displaying constitutive and regulated adipose tissue (cMAT and rMAT). The first adipose depot formed in BM is termed cMAT. rMAT develops with age and is distributed among other BM cells. Figure reproduced from Boroumand and Klip (2020). **(B)** BMAd displays distinct phenotypic characteristics within adipose tissue types. Figure reproduced from Sebo et al. (2019). **(C)** Selected pathways for adipogenesis upon exposure to insulin, dexamethasone and IBMX *in vitro*. Key: IR, insulin receptor; PKB, phosphokinase B; NRC, nuclear receptor complex; PDE: phosphodiesterase; PKA, phosphokinase A. Figure adapted from Toneatto et al. (2014). Illustration in **(C)** was created with Servier Medical Art (Servier, France).

1.3 Bone and energy metabolism

The presence of BMAd has been long considered as a passive filler of the BM cavity. However, recent studies suggest that BMAds actively participate in bone and energy metabolism (Li et al., 2019; Rendina-Ruedy and Rosen, 2020). For instance, human BMAds are responsive to insulin in promoting glucose uptake, but become impaired in diabetic subjects (Pham et al., 2020). This mechanism raises the possible protective function of BMAds against diabetes. Hyperglycaemic environment prefers adipogenesis over osteoblastogenesis, which infiltrates BM cavity. Ultimately, this condition weakens the bone through observable macro-architectural changes, which increases the risk of fractures and lowers bone quality (Napoli et al., 2016). The mechanism by which BMAds regulate bone metabolism in these scenarios remains poorly understood. To that end, research to elucidate bone marrow adiposity are on the rise.

At present knowledge, BMAds participate in bone metabolism by secreting molecules termed adipokines that locally and possibly distantly act on bone cells (Li et al., 2019). For instance, BMAds have been shown to secrete receptor activator of nuclear factor κ B ligand (RANKL) that binds to its receptor expressed by osteoclast precursors and may therefore enhance osteoclastogenesis (Muruganandan et al., 2020). On the contrary, secreted adiponectin has been shown to support bone formation by simultaneously upregulating osteoblastogenesis and inhibiting osteoclastogenesis in both *in vitro* and *in vivo* studies (reviewed in Lewis et al. (2021)). Several BMAd-secreted cytokines have been identified to act also on haematopoietic cells. For instance, interleukin factors (IL-3 and IL-8), C-X-C motif chemokine 12, colony-stimulating factor-2 and leukaemia inhibitory factors secreted by BMAds were able to support haematopoiesis in a co-culture system (Mattiucci et al., 2018). Adiponectin has also been shown to be anti-lymphoblastic in both *in vitro* (Yokota et al., 2003) and *in vivo* (Petridou et al., 2006). In summary, evidence from *in vitro* models suggests that BMAds regulate bone metabolism by either promoting or inhibiting the differentiation of other cells through the action of adipokines secreted.

Being energy-dense cells, it was previously thought that BMAds as a whole tissue act as an energy reservoir for the bone microenvironment. Unlike other adipose depots, however, BMAds do not respond to catabolic stimuli upon acute energy-deprived state

(Scheller et al., 2019), but becomes extremely anabolic upon chronic starvation (Cawthorn et al., 2016). Although it is not fully understood, adipogenesis in the latter scenario is hypothesised to be the survival energy source to save haematopoiesis at the last resort. The differences in lipid composition and gene expression are, therefore, a good start to elucidate the contrasting difference in metabolic behaviour between BMAds and other adipocytes (Attane et al., 2020; Rendina-Ruedy and Rosen, 2020).

The first link between BMAds and whole-body metabolism was discovered through the detection of IR in BMAds. Although inessential to BMAd survival, it was noted that the level of insulin linearly affects BMAd size (Qiang et al., 2016). It has been shown that mice with ablated insulin receptor reduced their BMAd size, while high insulin signalling in high-fat diet mice massively increased both number and size (Tencerova et al., 2018). With this knowledge, it is plausible that insulin modulates glucose uptake to induce lipogenesis in the bone marrow, hence promoting systemic glucose clearance as a protective mechanism against diabetes. Assessed with functional imaging, it was found that insulin enhances BM glucose uptake in healthy subjects, but not in obese or diabetic patients (Pham et al., 2020; Suchacki et al., 2020). Overall, these data suggest that BMAds respond to insulin and are linked to systemic metabolism. The state where BMAd becomes insulin-resistant and the mechanism by which metabolic diseases alter insulin sensitivity should be further addressed.

Unlike any other fat depots, BMAds follow a unique expansion during both extremes of caloric status. During a calorie-depleted state, such as caloric restriction and anorexia nervosa, the expansion of BMAds was evident (Bredella et al., 2009; Cawthorn et al., 2016). Although it was understood that BMAds resist lipolysis, the rationale of adipogenesis during this energy-deprived state remains speculative. It was later hypothesised by the same group that a point of turn from the metabolically inert BMAds to an energy-providing state exists when homeostasis could no longer be achieved. To that end, mice were exposed to both caloric restriction and exercise in a recently published study (McGrath et al., 2020). Similar to other fat depots, it was noted that exercise intervention had reduced adiposity in the underfed state, which confirms the first hypothesis of BMAds as an energy source. Interestingly, adiposity reduction from cMAT from the distal bones was evident, opposing the inertness as compared to rMAT. Altogether, this suggests that BMAds respond to catabolic stimuli upon caloric restriction. The molecular switch directing this change warrants further investigation.

1.4 Bone marrow adiposity and clinical significance

Over the course of a normal life, rMAT takes over BM environment and distinctly fills the cavity shortly after peak bone formation (Scheller et al., 2015). Affecting both genders, the increase of BM adiposity in females, however, is much more dramatic as compared to males, which was thought to be a consequence of menopause (Griffith et al., 2012). Later, it was discovered that oestrogen withdrawal in post-menopausal women increases BM adiposity and is reversible by the reintroduction of exogenous oestrogen. In fact, a study shows that oestrogen therapy had helped to improve the condition by reducing the number and size of BMAds (Syed et al., 2008). In older men, lower testosterone level is associated with higher BM adiposity (Mistry et al., 2018). In summary, the presence of sex hormone seems to inhibit marrow adipogenesis, as age-related reduction in hormone levels negatively affects BM adiposity.

Perhaps the central question is how an increase in BM adiposity affects general bone health. The infiltration of BMAds exhausts the osteogenic potential of BMSCs, as adipogenesis is favoured over osteoblastogenesis. Consequently, the bone formation rate is lowered to the point of a clinically relevant skeletal fragility and reduced bone mineral density (Kawai et al., 2012). In their review, a high inflammatory state courtesy of BM adipokines and free fatty acid severely inhibited osteoblastogenesis, as opposed to the pro-osteoblastic adiponectin. Low bone mineral density and high marrow adiposity has been linked with high fracture incidence in both healthy (Shen et al., 2007) and diabetic individuals (Rzonca et al., 2004). Although the effect on haematopoiesis is still under investigation, reports have shown that marrow adiposity enhances myelopoiesis (reviewed in Patel et al. (2018)). In the skeletal context, BMAds secrete RANKL to the BM environment, which was shown to increase bone resorption mediated by osteoclastogenesis (Fan et al., 2017).

Interestingly, not all cases of high BM adiposity are accompanied by low bone mineral density. Although obesity increases BM adipogenesis in general, the majority of obese individuals revealed normal to larger areal bone mineral density according to dual-energy x-ray absorptiometry results (Evans et al., 2015). It was proposed that the high bone strain due to a heavier mechanical load and different exposure to adipokines in a high adiposity environment stimulates bone formation. For instance, the adipokine leptin has been

shown to enhance mineralisation in primary osteoblast cultures assessed by the alizarin staining method (Reseland et al., 2001). However, bone architecture including radial cortical area, total bone cross-sectional area and periosteal circumference was compromised in the obese subjects, compared to non-obese individuals (Pollock et al., 2007). Taken together, although bone mineral density is high in the obese subjects, the functional composition of the bone may be more predictive to assess overall bone health.

In the quest to reverse BM adiposity, the development of biological and non-biological interventions is on the rise. Among these options, exercise has been shown to reduce BM adiposity and, hence, restore skeletal health (summarised in Pagnotti and Styner (2016)). To assess whether pathological BM adiposity could be reversed as well, Styner and colleagues (2015) challenged rosiglitazone-supplemented mice to exercise for six weeks. As expected, massive loss of BMAds was seen from femoral micro-computed tomography images. Further, exercise increased bone fraction volume when compared to the sedentary group. Therefore, regardless of physiological (age or hormonal status) or pathological origin of BMAds, exercise as an intervention is able to restore skeletal health by reducing BM adiposity.

The mechanism by which exercise reduces the number/amount of BMAds remains unknown. Upon mechanical stimulation, the bone-muscle axis is activated by mechanosensitive osteocytes and osteoblasts which, in turn, secrete factors to the BMSC microenvironment directing osteoblastogenesis and ultimately reduce adipogenic commitment (Robling and Turner, 2009). Mechanical stretching and exercise downregulate PPARG on BMSCs *in vitro* and *in vivo*, respectively, thereby providing a possible mechanistic link between exercise and reduced adipogenesis (David et al., 2007). It would therefore be interesting to dissect the mechanistic fate of the existing BMAd population upon exercise, whether they enter cellular senescence through delipidation (Styner et al., 2017), energy-providing state, dedifferentiation, transdifferentiation, or any of the combination thereof. Such knowledge would strengthen the notion of which BMAds are responsive and adaptive to physical stimuli.

1.5 Future direction towards bone marrow adiposity research

The field of bone marrow adiposity is relatively new. At present, meticulous work on the standardisation of working terminologies (Bravenboer et al., 2019) and methodologies (Tratwal et al., 2020b) is being developed to standardise research communications across groups. Isolating BMAds from within the BM is difficult. This prompts investigators to differentiate BMSCs, which is easier to obtain, into adipocytes *in vitro*. However, the method by which BMSCs are induced to adipocytes is not standardised, resulting in adipocytes that may deviate from naïve BMAds (Cawthorn et al., 2016; Fayyad et al., 2019). The degree of induction varies greatly and is often dramatised through the use of potent inducers, such as rosiglitazone, among others. Therefore, it is not known whether *in vitro* differentiation would fully represent *in vivo* BMAds both descriptively and functionally. Ultimately, comparative studies of BMAds *in vivo* and adipocytes differentiated *in vitro* are of great significance to conclude the potential of the differentiation model as a starting material in bone marrow adiposity research.

Inter-species and spatiotemporal regulation of BMAds often contradicts the observations among identically-designed studies (Scheller et al., 2015). Such variation raises further questions about which BMAd population is the main player in bone regulation. In addition, methods to obtain BMAds *in vivo* are currently underdeveloped. To complicate further, the knowledge of surface markers on both BMSCs, pre-BMAds and mature BMAds is currently superficial (Li et al., 2018). BMAds, like other fat cells, are extremely fragile and mishandling often burst the cells. Due to the non-adherent nature, raising primary BMAds long-term *in vitro* is still in early development even after successful isolation. Ultimately, it is exhaustive and difficult to quantitate BMAds from most imaging-based studies, most notably from the light microscopy modality.

Current clinical assessment of marrow adiposity is performed through a series of radiological imaging (reviewed in Singhal and Bredella (2019)). Magnetic resonance imaging setup remains the most popular choice by separating water and fat signal, thereby providing information on total bone adiposity although lacking the structural detail. Further improvement on this end has introduced a gold standard single-voxel proton magnetic resonance imaging, which allows a regional fat distribution mapping based on the signal intensity from different skeletal regions. However, none of the existing medical

imaging setups are able to resolve cellular or tissue resolution of BMAds as a whole tissue, such as BMAd size distribution and morphology. Development on this end is currently ongoing by starting from *ex vivo* and *in vitro* imaging setups.

The morphology of BMAds can be assessed through *ex vivo* and *in vitro* imaging. A simple routine histological staining of bone sections like haematoxylin and eosin (HE) is often sufficient for *ex vivo*-based analysis. However, alcohol treatment during the sample preparation causes delipidation, which destroys the general structure of BMAds. Ultimately, this leaves the only preserved portion of the thin cytoplasm stained by eosin, coining the term 'ghost adipocytes'. It is rather difficult to extract information from this model, as quantitation of ghost adipocytes is usually done through manual and laborious estimation that is rather subjective. Further, small adipocytes are left uncounted and often confused with histological artefacts or marrow space. In addition, small BM vasculature like nerve and blood vessels can be mistaken as adipocytes, especially when adiposity is high in that region. To that end, a digital image analysis method has been developed to semi- or even fully-automatically estimate bone marrow adiposity based on the feature of ghost adipocyte taking the background colour (summarised in Tratwal et al. (2020b)).

Adipocytes, in general, can also be visualised *in vitro* to understand the morphological features. Lipid droplets can be imaged using bright field microscopes with or without staining aid, although the former is preferred for specific detection. Common staining method targeting neutral lipids like oil-red-O (ORO) is the gold standard for this purpose, and to be quantitated digitally using the same colour-based principle, as described in the previous section (Eggerschwiler et al., 2019; Kraus et al., 2016; Yuan et al., 2019). However, quantitation using water-based staining methods are often miscounted due to dye precipitation and non-specific binding. To that end, specific fluorescent probes are now preferred to accurately stain adipocyte features like the lipid characteristic or a surface marker perilipin (reviewed in Fam et al. (2018)). Discrete and specific signals from these fluorophores enable accurate and reliable quantitation up to cellular (adipocyte morphology) and even sub-cellular level (lipid characteristic).

Lastly, it is speculated that BMAds display a distinct character from other fat depots. By secreting adipokines, BMAds may regulate skeletal homeostasis. However, the knowledge is superficial and rather descriptive. Little is known about the mechanism by which adipokines exerts their functional role locally and possibly distantly. At present,

defining the methodology to isolate and culture primary BMAds is of great importance as a starting phase. The low and impure yield of primary BMAds warrants improvements to emerge. Further, the fragile nature of adipocyte restricts further handling, and successful cultures using the ceiling method are rather short-lived and complicated (Zhang et al., 2000). Currently, the development of a 3D culture model using bio-scaffolds shows a promising result (Fairfield et al., 2019) and may one day overcome this limitation and direct translation in dissecting the molecular mechanism of BMAds as functional fat depots. **Figure 3** summarises the prospect of bone marrow adiposity research.

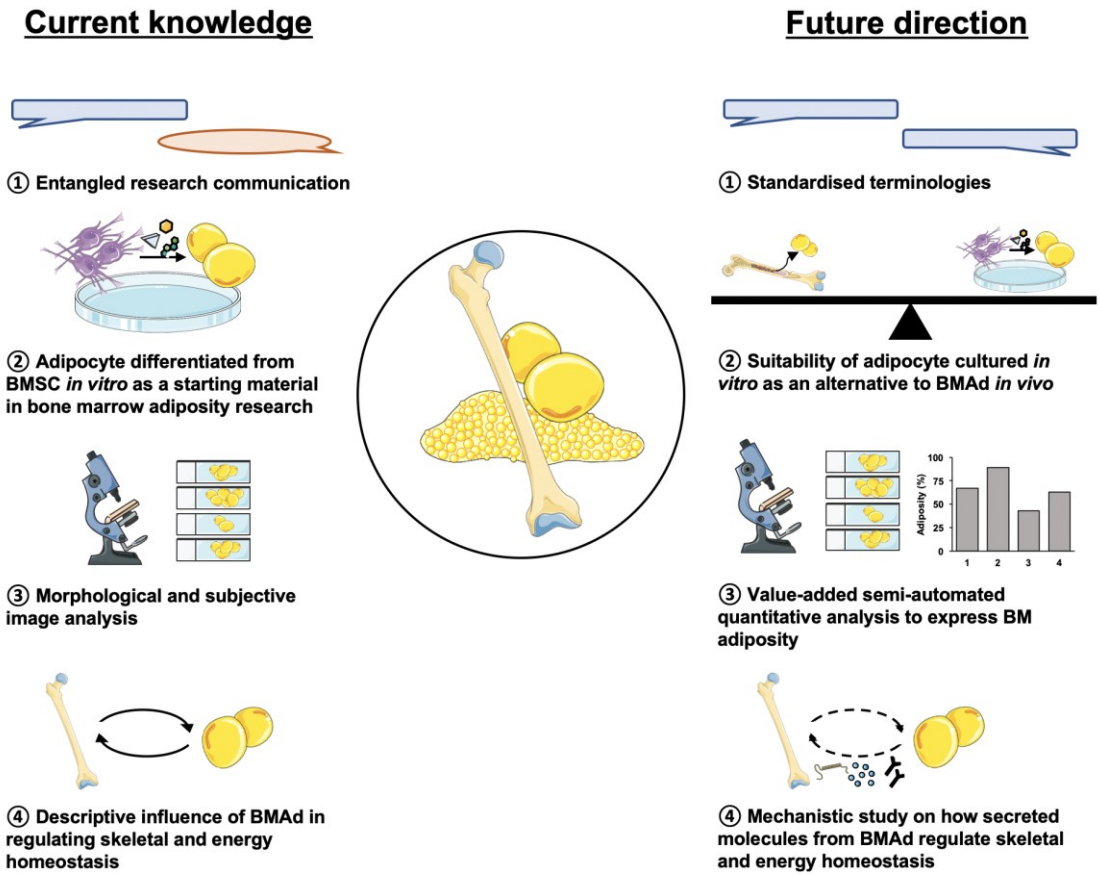

Figure 3. Current knowledge and prospect towards bone marrow adiposity research. The illustration is created with Servier Medical Art (Servier, France).

CHAPTER II
RESEARCH AIMS AND HYPOTHESES

The present knowledge of BMAds and their presumptive roles in regulating bone and energy metabolism warrant further descriptive and mechanistic research to emerge. This study will focus on fundamental questions in describing the current methodology of BM adiposity research. The following aims are set for the study:

1) To develop an adipogenesis differentiation model from BMSCs *in vitro.*
2) To develop and evaluate semi-automated image analysis workflows capable of quantitating BM adiposity from acquired bioimages.

Overall, this research will employ cell-based approaches to facilitate the proposed aims. We hypothesise that the morphological and mRNA expression profile of the adipocytes formed *in vitro* would confirm the adipogenesis induction. The mRNA expression level would correlate to the adipocytes morphology linearly. From the image analysis setup, we aim to develop a colour-based segmentation method that could detect BMAds based on their distinctive appearance, the circular morphology. We hypothesise that a working algorithm that could differentiate other circular objects apart from the target in question would provide a specific and reliable quantitation method.

Of importance, this study may strengthen the ongoing optimisation theme of the newly-formed society for bone marrow adiposity research by contributing a standard methodological work for the field to grow. The outcome of the first aim may direct further improvements to the point of an establishment towards a reliable working model. The direction towards automation in image analysis may reduce inter-user variation in reporting, which has been the primary goal to harmonise research communication across identically-designed studies. Ultimately, we hope that the present study will facilitate further research to emerge.

CHAPTER III

MATERIALS AND METHODOLOGIES

In this study, we utilised mostly cell-based approaches to characterise adipocytes differentiated from BMSCs *in vitro*. We compared adipocyte-specific messenger ribonucleic acid (mRNA) expression patterns and the morphology to evaluate our differentiation model as a potential alternative to primary BMAds. Finally, we developed a semi-automated approach to quantitate BMAds from histological bone sections to estimate whole-marrow adiposity. **Figure 4** outlines the design of our methods.

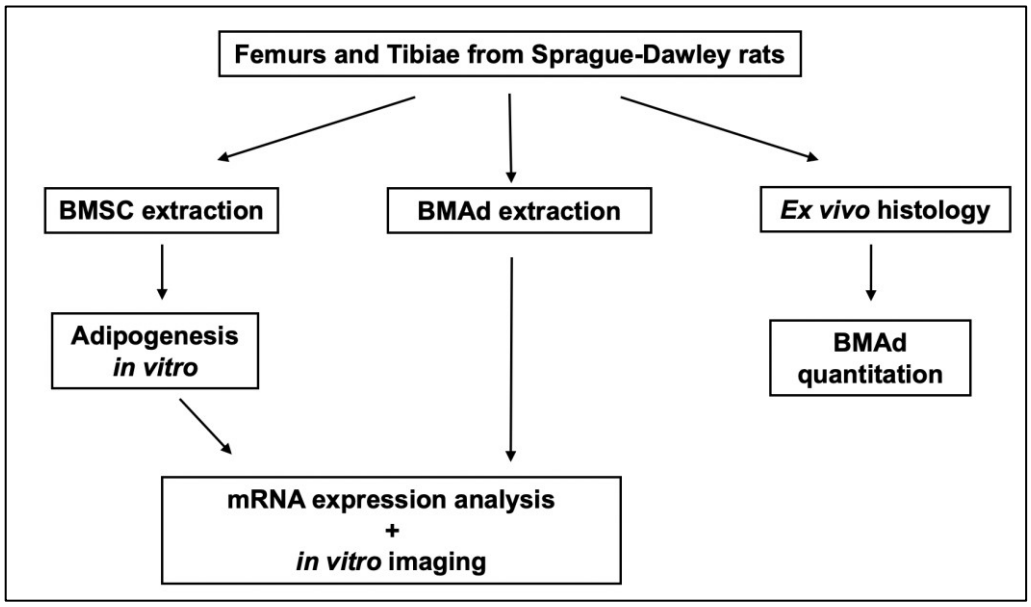

Figure 4. Overview of overall research design.

3.1. Isolation, culture and differentiation of bone marrow stromal cells

Femurs and tibiae from four-week-old female Sprague-Dawley (SD) rats were harvested to extract BMSCs according to the centrifugation (Maridas et al., 2018) or marrow flush (Huang et al., 2015) method, as previously described. Briefly, demuscularised and marrow-exposed bones were placed into an insert adapted to a collection tube and followed by a brief centrifugation at 7,500x g for 15 s to extract total BM cells. Alternatively, BM cavity was flushed with culture medium using a 25G needle until bones appear pale. Cells were grown undisturbed for one week and supplemented with basal medium containing alpha-MEM, 15% foetal bovine serum, 1% penicillin-streptomycin, 10^{-2} M HEPES buffer, 2.50 µg/mL amphotericin B, 2 x 10^{-3} M glutamax and 10^{-8} M

dexamethasone (Sigma Aldrich, USA). Medium components were obtained from Gibco (ThermoFisher Scientific, USA), unless specified otherwise. Approximately 48 hours after seeding, non-adherent haematopoietic cells were removed by washing with sterile phosphate-buffered saline solution. The use of animal experimentation in this study was approved by the local ethical committee and provided by the Central Animal Laboratory (University of Turku, Finland).

BMSCs were seeded with an initial density of 2.1 x 10^4 cells/cm^2 and directed for adipogenesis. Two adipogenic cocktails were evaluated for the differentiation model containing 10 µg/mL insulin (Sigma Aldrich, USA), 10^{-6} M dexamethasone (Sigma Aldrich, USA), and either 5 x 10^{-4} M IBMX (Sigma Aldrich, USA) or 0.05% dimethyl sulfoxide (DMSO) vehicle. Cells were supplemented with basal medium containing 10% foetal bovine serum without amphotericin B. The study was performed in three replicates. Cell growth was monitored daily and the medium was replaced every three days. Half of the medium was removed and replaced with an equal removal volume containing twice the concentration of the adipogenic cocktail.

3.2. Isolation of primary bone marrow adipocytes

Primary BMAds were isolated with a modified collagenase digestion method (Scheller et al., 2015). Briefly, femurs and tibiae from a 19-week-old female SD rat were extracted and cut with a rotary tool (Dentsply Sirona, USA) and diamond disc (#911H104180; Komet dental, Germany) to expose the marrow cavity at approximately below the trabecular region. Bones were placed in the collection tube containing 1 mL Hank's balanced salt solution (8.10 g NaCl, 0.4 g KCl, 600 mg Na_2HPO_4, 600 mg KH_2PO_4, 1 gr glucose, 350 mg $NaHCO_3$, 10 mg phenol red), 10^{-2} M HEPES (ThermoFisher Scientific, USA), 3% bovine serum albumin, 1 mg/mL collagenase A (Roche, Germany), 0.25% sodium citrate and 50 U/mL heparin (Grenier Bio-One, Austria). BM was extracted following the centrifugation method at 3,000x g for 2 minutes. The solution was incubated in a water bath at 37°C for 20 minutes with frequent agitation. To liberate BMAds, the solution was then incubated for another 5 minutes without agitation. The solution was centrifuged to pellet BM cells at 800x g and room temperature for 10 minutes. The top layer was collected for imaging by Hoechst and BODIPY staining (**section 3.4**) to confirm the presence BMAds.

3.3. Adipocyte-specific mRNA expression analysis

Primer pairs (Integrated DNA Technology, USA) targeting mRNA sequence cyclophilin B (CYCB), beta-actin (ACTB), PPARG, CEBPA, ADIPOQ, FABP4 and UCP1 were designed with the aid of Primer-BLAST (National Centre of Biotechnology Information, USA) under the following criteria: (1) Tm differences <1°C; (2) PCR product length <200 base pairs; and (3) span exon-exon boundary. **Table 1** outlines the primer details used in this study. With the exception of CYCB, newly designed primers were tested and optimised with the suggested positive control of rat adrenal or adipose tissue total RNA (Zyagen, USA) using CFX96 Real-time PCR Detection Systems (Bio-Rad, USA). Primer specificity was assessed by agarose gel electrophoresis. Briefly, 0.5 µL Midori Green Direct (Nippon Genetics Europe, Germany) was added into the PCR products and loaded into 2.5% agarose gel (BioNordika, Sweden). Fifty-bp DNA ladder (ThermoFischer, USA) was added as a size reference. The gel was electrophoresed in Tris-Borate-EDTA buffer at 100V/100mA for an hour and then imaged with FastGene FAS-Digi Pro imaging system (Nippon Genetics Europe, Germany). The efficacy of each primer was assessed by plotting a standard curve of logarithmic dilution series of cDNA versus threshold cycle to obtain the efficiency as calculated from **equation 1** according to the manufacturer protocol.

$$\%\ \text{Efficiency} = \left(2 - \left(10^{-\frac{1}{\text{slope}}}\right)\right) \times\ 100\% \quad \text{--- } \mathbf{equation\ 1}$$

Total RNA from BMSCs and adipogenic cultures on day-0 and day-3, 6, 9, 12, 15 and 18, respectively, was isolated with NucleoSpin RNA Plus kit (Macherey-Nagel, Germany) following the manufacturer protocol. Briefly, cells were lysed using the supplemented lysis buffer and purified from genomic DNA prior to RNA isolation. For the subsequent reverse-transcribed quantitative polymerase chain reaction (RT-qPCR) flow, 500 ng of extracted RNA was reverse transcribed into cDNA using a thermal cycler (Eppendorf, Germany). To monitor and quantitate the reaction, SYBR green qPCR kit (ThermoFisher Scientific, USA) was used in this study according to the manufacturer protocol. The mRNA expression was normalised to the reference genes CYCB or ACTB and compared to undifferentiated BMSCs (day-0 culture). Changes in the expression are presented in fold changes following the $2^{-\Delta\Delta Ct}$ or known as the Livak method, as

previously described (Livak and Schmittgen, 2001). For the mRNA expression analysis, three biological replicates and two technical replicates were performed.

Table 1. Primer sequence used in this study.

Genes		Sequence (F, forward; R, reverse)	Primers annealing temperature (°C)	Predicted product size (base pairs)
CYCB	F	ACCTGTAGGACGAGTGACCT	59.6	187
	R	GCTCTTTCCTCCTGTGCCAT	60.03	
ACTB	F	CCCGCGAGTACAACCTTCTTG	61.27	71
	R	GTCATCCATGGCGAACTGGTG	61.61	
PPARG	F	AACTCTGGGAGATCCTCCTGT	59.64	90
	R	CTGTGTCAACCATGGTAATTTCTTG	58.85	
CEBPA	F	CTGGCTCTGGGTCTGGAAAG	60.4	81
	R	GAGAAGGAAGCAGTCCACCC	60.4	
ADIPOQ	F	CCTGGTCACAATGGGATACCG	60.48	93
	R	CTTAGGACCAAGAACACCTGCG	61.19	
FABP4	F	CATAACCCTGGATGGTGGGG	59.81	115
	R	GCCTTTCATGACACATTCCACC	60.09	
UCP1	F	AGACAGAAGGATTGCCGAAACT	59.96	196
	R	TGCCCAATGAATACCGCCA	59.7	

3.4 Adipocytes imaging in vitro

BMSCs from 4-week-old SD rats were seeded with the initial density of approximately 2.6 x 10^4 cells/cm^2 and induced for adipogenesis with the same setup as in **section 3.1**. Cells were fixed with 3.6% formaldehyde prior to a 5-minute staining with ORO (Sigma Aldrich, USA) to highlight accumulated intracellular lipid droplet and followed by a haematoxylin counterstain to visualise basophilic structures. Alternatively, fluorescent-based imaging of adipocytes was performed using 0.5 µg/mL BODIPY 493/503 (Invitrogen, USA) and 5 µg/mL Hoechst 33258 346/460 (Sigma Aldrich, USA) to stain lipid droplet and nucleus, respectively. The nuclear staining was excluded from our live-cell imaging setup. EVOS M5000 Imaging System (Invitrogen, USA) was used to image the cells with either bright field, DAPI (357/447), GFP (470/525) mode, or any of the combinations mentioned. Representative images from the middle of each well were acquired for the analysis.

Semi-automated quantitation methods by ImageJ (Schindelin et al., 2012) were developed from both water-based and fluorescent-based imaging setups. The area of ORO staining *(ORO.Ar)* was estimated and compared to the total haematoxylin area *(H.Ar)* to calculate the adiposity *in vitro* according to **equation 2**. From the fluorescent setup, the nuclear pixels that overlapped with the BODIPY area (lipid droplets) helped us to quantitate the proportion of adipocytes obtained from the differentiation *in vitro* based on **equation 3**. Briefly, the logical operator 'AND' was used to bring the pixel value of co-localising DAPI (nucleus) and GFP (lipid droplets) pixels to define adipocytes. Segmented lipid droplets were expanded by a 10-pixel disc to allow the superimposition of nuclear objects for detection through the binary operator of 'dilation'. The script containing commands used in this approach is published in **Appendix 1.**

$$\%\text{Adiposity} = \frac{ORO.Ar}{H.Ar} \times 100\% \quad \textbf{--- equation 2}$$

$$\%\text{Adipocyte proportion} = \frac{N_{BODIPY^+HOECHST^+}}{N_{HOECHST^+}} \times 100\% \quad \textbf{--- equation 3}$$

3.5 Bone marrow adipocytes quantitation by histology

Femurs and tibiae of a 16-week-old female SD rat were harvested for the histology study. Bones were fixed with 10% neutral buffered formalin solution and 70% ethanol for 2 days and overnight, respectively. Fixed samples were then decalcified in 14% EDTA solution for 16 days with a solution change twice a week. Samples were then stored in 70% ethanol before submission to the Histology core facility of the Institute of Biomedicine (University of Turku, Finland) for embedding, sectioning and staining. Samples were longitudinally trimmed approximately 50% to expose the marrow cavity and sectioned at 4 μm thick. Four slides were stained by HE to visualise bone marrow cellularity. Slides were imaged with a slide scanner Pannoramic 1000 (3DHISTECH, Hungary).

Bone marrow adipocytes were quantitated semi-automatically with the aid of image analysis software. We first validated two popular histological image analysis software QuPath (Bankhead et al., 2017) and ImageJ. An open-source, additional plugin of MarrowQuant was used for the QuPath quantitation as described previously (Tratwal et

al., 2020a). Briefly, MarrowQuant follows a multi-segmenting algorithm allowing the detection of adipocytes (AdipoQuant), nucleated cells, haematopoietic cells and mineralised bone from the image by classifying the colour nature of each pixel according to the object of interest. For instance, BMAds were segmented based on the background colour due to the delipidation upon alcohol exposure during sample processing. The algorithm then registered every background-coloured pixel to create a mask that defined adipocyte from other objects. Finally, user-defined parameters, such as size and circularity, assigned the detected object as BMAd. In this study, the standalone plugin AdipoQuant was used to solely quantitate BMAds.

A validation set containing five 0.25 mm^2 regions was randomly selected and drawn from every sample (N=20) which included the marrow region, vascularised marrow, marrow trabeculae, marrow with histological artefact and cortical region. BMAds were manually counted to act as a reference comparator to AdipoQuant- and ImageJ-based quantitation. Tissue boundaries, background and artefact regions were drawn from each area as required by the algorithm. The following criteria were applied in analysing the image: (1) BMAds sized 200–4000 μm^2, (2) circularity between 0.4–1.0, (3) exclusion on edge-detection, and (4) three down-sampling rate. **Figure 5A** summarises the workflow of the image analysis by AdipoQuant.

For ImageJ-based quantitation, the image was segmented to separate object and background. The segmented image was then inverted to define the background as the count parameter, as BMAd took most of the background colour. To distinguish marrow vasculatures as suspected BMAd, a morphological operation of 'opening' was performed. A disk-shaped element with a user-defined radius was applied to intentionally 'break' the detected vessels and, therefore, be excluded in the particle count. Finally, the following parameters were applied to count the object automatically: (1) BMAd sized 200–4000 μm^2, (2) circularity between 0.4–1.0, and (3) exclusion on edge-detections. **Figure 5B** summarises the workflow of the image analysis by the ImageJ method. The script used in this study is published in **Appendix 2**. Lastly, we calculated the error rate to evaluate our quantitation workflow according to **equation 4**.

$$\text{Error rate (\%)} = \frac{|N_{manual} - N_{automated}|}{N_{manual}} \times 100\% \quad \textbf{--- equation 4}$$

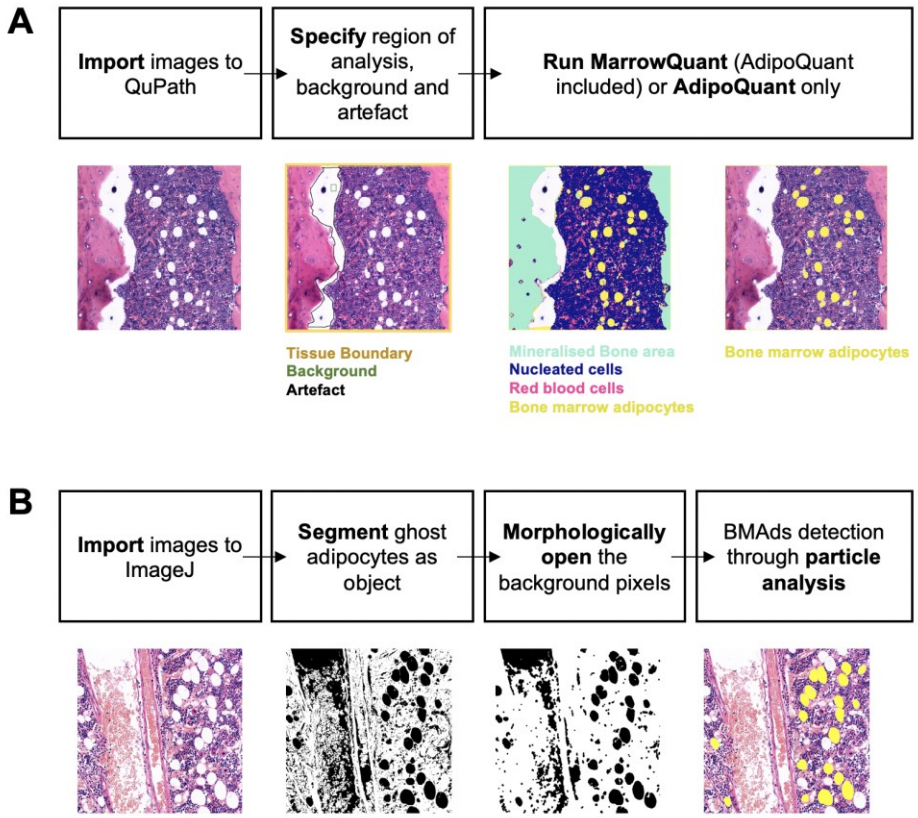

Figure 5. Workflow of BMAd quantitation from histological images. (A) In MarrowQuant, the user first specifies the region of analysis, background colour and artefacts. The algorithm then creates masks to detect mineralised bone area, nucleated cells, adipocyte (also called AdipoQuant) and red blood cells. The algorithm analyses the shape of the detected objects and generates the report. Figure adapted from Tratwal et al. (2020a). **(B)** ImageJ-based detection starts by segmenting the input image to separate BMAd-like structures (white colour) from other objects. The segmented image is then morphologically opened to destroy detected vascular structure. Particle analysis quantitates the amount of BMAd according to the parameters set by the user.

3.6 Data and statistical analysis

Data are presented in mean ± SD. Adipocyte shape descriptor and units of reporting such as adipocyte area (*Ad.Ar*) and density per area or the number of adipocytes to marrow area (*N.Ad/Ma.Ar*) were used as recently suggested by the international working group (Bravenboer et al., 2019). Student's *t-test* was performed to determine statistical significance between groups. The following denotations were used to express statistical significance: $p< 0.05$ (*); $p< 0.01$ (**); $p< 0.001$ (***) and $p< 0.0001$ (****). Prism v.9.0 (GraphPad Software, USA) was used to present and statistically analyse the data.

CHAPTER IV
RESULTS

4.1 IBMX upregulated the expression of adipocyte-specific mRNAs, but failed to facilitate the intracellular lipid accumulation and typical morphological changes

We first evaluated the specificity and efficiency of the primers used in this study. As shown in **Figure 6A**, a single band of amplicons from each primer pair was seen from the agarose gel, indicating a specific binding and amplification of the desired product. In general, the size of each band corresponds to the predicted product size (**Table 1)**. We did not detect bands from our negative control samples (without template) (**Fig. 6B**), suggesting a specific binding of the primers to the target sequence without a primer dimer formation or off-target binding. Next, we evaluated the efficiency of the primer pairs (**Fig. 6C**) according to the manufacturer guideline (Bio-Rad, USA). With the exception of CEBPA (110.4%), ADIPOQ (112.2%), FABP4 (111.8%) and UCP1 (110.2%) primers, three of the primers targeting CYCB, ACTB and PPARG were within the suggested efficiency range (90 – 105%). Upon optimisation, the primers used in this study have a final annealing temperature of 58°C, except for CYCB (60°C).

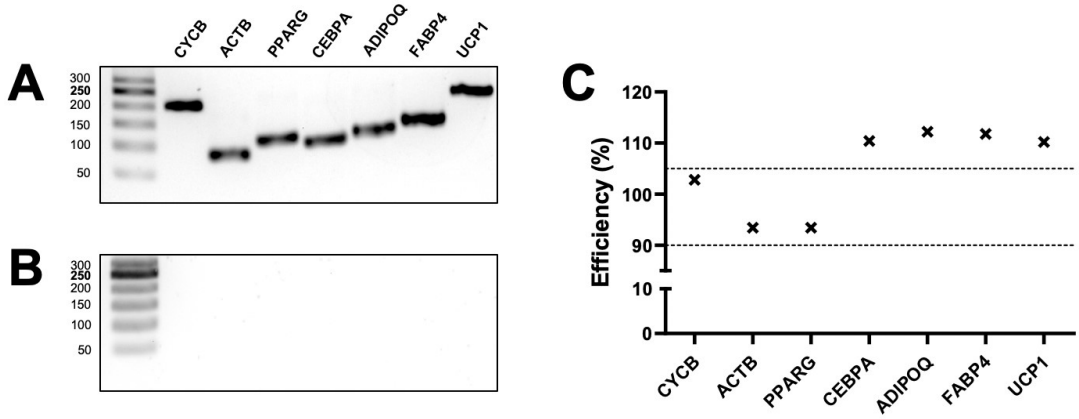

Figure 6. Specificity and efficiency of the primer pairs used in this study. Single-bands of amplicons were distinctly sorted on agarose gel **(A)**, but not from the **(B)** negative control samples (H_2O). The size of the DNA ladder in base pairs is annotated on the left side of the image. **(C)** The efficiency of the primer pairs in doubling the target sequence per cycle. Dotted lines represent the suggested range of efficiency according to Bio-Rad guidelines. Original agarose gel images can be found in **Appendix 3**.

Next, we evaluated the effect of two different BMSCs isolation methods and two adipogenic cocktails on adipogenesis *in vitro*. The undifferentiated BMSCs from both isolation methods were used as a reference to the adipocyte-specific gene expression normalised to the CYCB expression. On day 6 of differentiation, the mRNA expression level of PPARG, ADIPOQ and FABP4 in the culture obtained from the centrifugation method were higher compared to the flush method **(Fig. 7A)**, regardless of the induction model (PPARG, $p= 0.0168$ versus $p< 0.0001$; ADIPOQ, $p= 0.0032$ versus $p< 0.0001$; FABP4, $p= 0.0073$ versus $p= 0.0003$ from cultures with and without IBMX supplementation, respectively). Among the centrifugation models, we observed a statistically significant increase in the mRNA expression level of PPARG ($p= 0.0332$), ADIPOQ ($p= 0.0033$) and FABP4 ($p= 0.0188$) in IBMX-supplemented cultures compared to those without IBMX. On average, we observed more than 50- and 20-fold increase of ADIPOQ and FABP4, respectively, from BMSCs obtained by the centrifugation model compared to the reference. Contrastingly, BMSCs obtained by the flush method without IBMX supplementation downregulated their adipocyte-specific markers when compared to the undifferentiated control.

Interestingly, the mRNA expression analysis and imaging data were contradictory. We did not detect adipocyte formation *in vitro* in the IBMX-supplemented group **(Fig. 7B and E)**, but evidently in our IBMX- cultures **(Fig. 7C and F)**. Further, the other cells from the IBMX-supplemented cultures were larger in size (**Fig. 7B**), compared to those without IBMX (**Fig. 7C**). Neutral-lipid staining by ORO or BODIPY confirmed the multilocular lipid droplets and morphology resembling brown adipocytes. We took the ratio of *ORO.Ar* and *H.Ar* to estimate the adiposity area *in vitro*. As expected, we found a statistically significant difference in adiposity *in vitro* between IBMX+ (0.20±0.11%) and IBMX- (8.25±1.74%) cultures ($p< 0.0001$). The precipitates of ORO during the staining process interfered with our image analysis flow and resulted in a nonspecific false-negative lipid detection. To that end, we developed a staining method with fluorophores targeting the double-stranded DNA and neutral lipid **(Fig. 7E and F**). Based on this specific detection, we were able to estimate the rate of adipogenesis based on the co-localising nucleus within the detected lipid region. We found that 13.18±4.16% of BMSCs from the IBMX- had differentiated into adipocytes *in vitro* **(Fig. 7G)**. Taken together, we recommend BM extraction following the centrifugation method and exposed BMSCs to 10 µg/mL insulin and 10^{-6} M dexamethasone for adipogenesis *in vitro*.

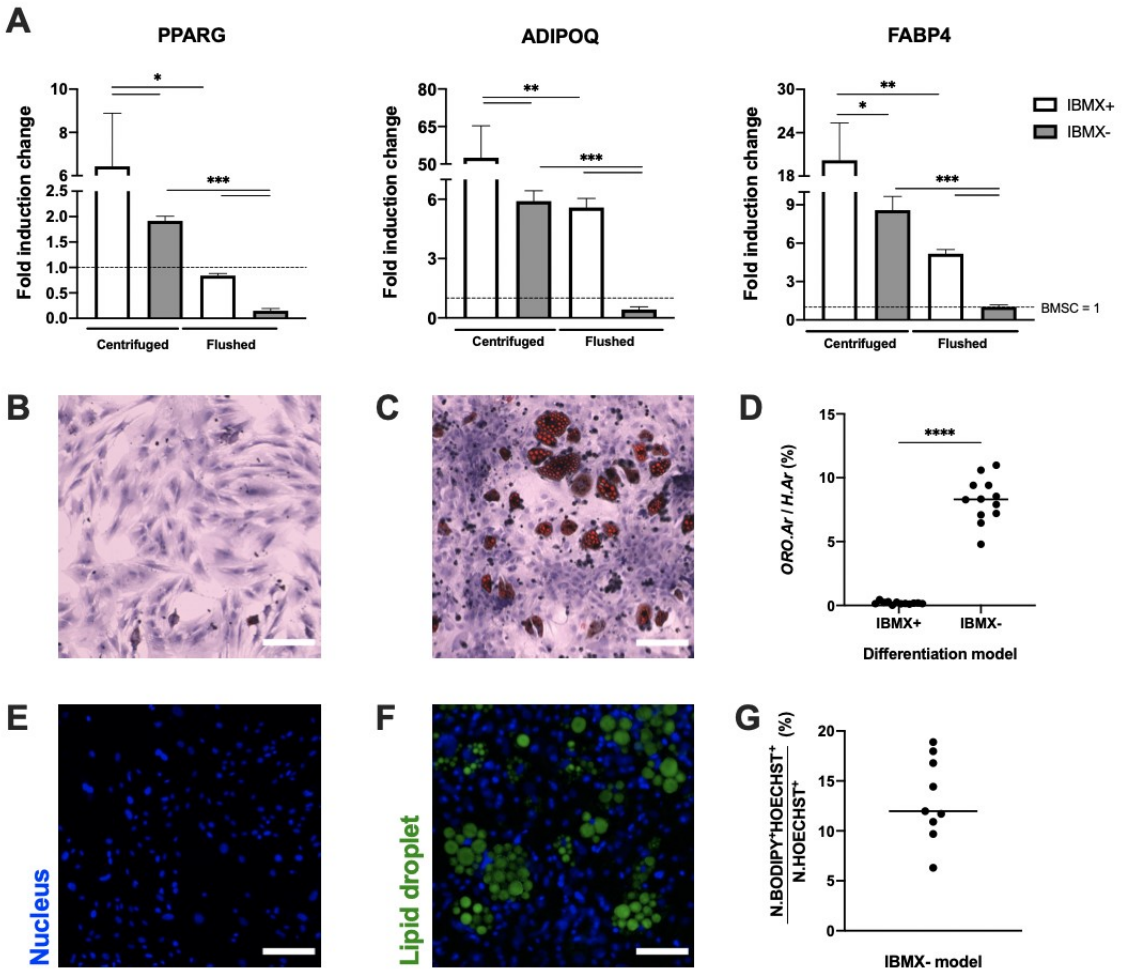

Figure 7. IBMX upregulated the adipocyte-specific mRNA expression, but failed to induce morphological changes. (A) Adipocyte-specific gene expression analysis of the *in vitro* model on day 6 of differentiation. The expression profile is normalised to a reference gene CYCB, and compared to the undifferentiated BMSCs (set as 1, shown as dotted lines). Oil-red-O and haematoxylin staining of **(B)** IBMX+ and **(C)** IBMX- culture. **(D)** Quantitation of adiposity, based on the area of staining *in vitro* (N= 12 per group). Nuclear and lipid-droplet staining of **(E)** IBMX+ **(F)** and IBMX- culture **(G)** Ratio of adipocytes to undifferentiated BMSCs (number of nuclei) *in vitro* (N= 9). Scale bar: 100 µm. The quantitation was limited only to the representative images measuring 0.545 mm^2.

4.2. Adipocytes differentiated in vitro display a distinct adipocyte profile

In order to characterised the adipocytes from the optimised *in vitro* differentiation model, we induced adipogenesis from BMSCs for 18 days and assessed the adipocyte-specific mRNA expression profile every three days. Compared to the undifferentiated control (day 0), the expression of adipocyte-specific genes was increasingly upregulated, and peaked after 18 days of adipogenic differentiation (**Fig. 8A**). The expression levels of the transcription factors PPARG and CEBPA were significantly upregulated on day 15 compared to the control ($p= 0.0038$ and $p= 0.02$, respectively). In addition, the adipocyte-specific markers ADIPOQ and FABP4 were significantly upregulated as early as 6 ($p< 0.0001$) and 3 ($p=0.018$) days following induction, respectively. Compared to the undifferentiated control, fold changes of mRNA expression were the highest for ADIPOQ and FABP4 by the end point of differentiation. We noticed a doubling in mRNA expression of the transcription factors PPARG ($p= 0.018$) and CEBPA ($p= 0.02$) on day 18, compared to the baseline control.

Next, we followed the morphological changes of differentiating BMSCs *in vitro* using a live-cell imaging setup. We found an inconsistent rate of morphological transition of BMSCs to adipocytes (data not shown), but representative images showed a gradual increase in the lipid droplet size from day 3 to 18, in general **(Fig. 8B)**. Representative adipocytes were not a longitudinal image series of a specific single cell. We initially thought that a cluster of lipid droplets in a defined enclosure was a representation of a single adipocyte. However, co-staining with Hoechst showed multiple nuclei within the lipid droplets cluster **(Fig. 9A)**. This suggests multiple adipocytes were in close proximity to each other. The phase contrast image in **Figure 9A** shows a cytoplasmic extension of the adipocyte cluster containing most of the nuclei within that region.

Our preliminary data suggests that primary BMAds isolated from rat BM were morphologically different from the adipocytes differentiated *in vitro*. **Figure 9B** shows a large unilocular lipid droplet representing a single BMAd. Further, we also noticed a crescent-shaped nucleus near the periphery of the cell, between lipid droplet and plasma membrane. Taken together, BMAds resemble classical white adipocytes in morphology. Due to the morphological resemblance between *in vitro* differentiated adipocytes and multilocular brown adipocytes, we checked the mRNA expression of UCP1, a

thermogenic hallmark protein for brown adipocytes. We found that the adipocytes differentiated *in vitro* did not express UCP1 **(Fig. 9C)**.

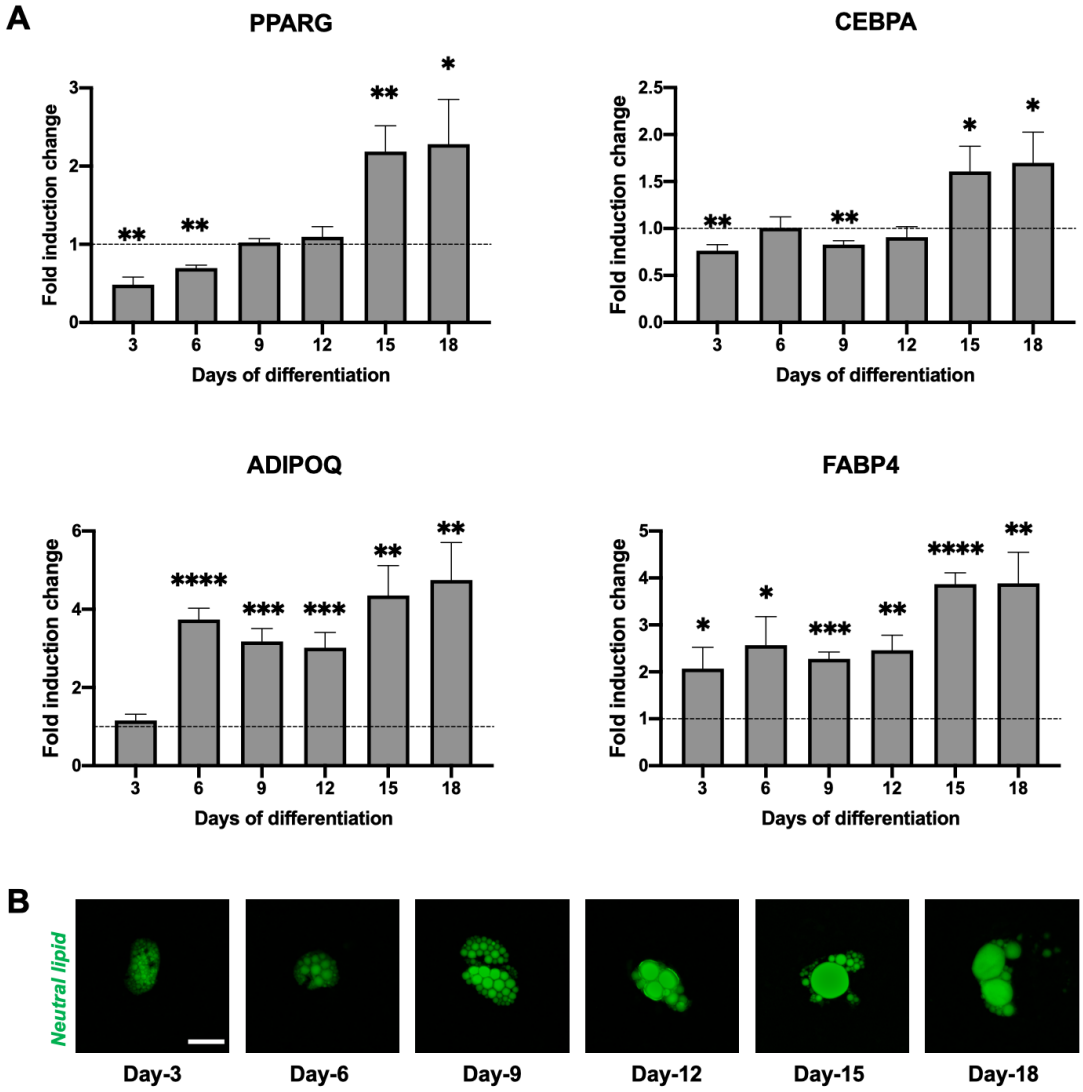

Fig 8. Adipocytes differentiated from BMSCs *in vitro* reflects a bona fide adipogenesis. (A) Temporal adipocyte-specific mRNA expression analysis of the adipogenic cultures across different time points. The expression is normalised to CYCB expression, and compared to the undifferentiated BMSCs (set as 1, shown as dotted lines). **(B)** Temporal increase in lipid-droplet size confirms the formation and maturation of adipocytes *in vitro*. Scale bar: 50 µm.

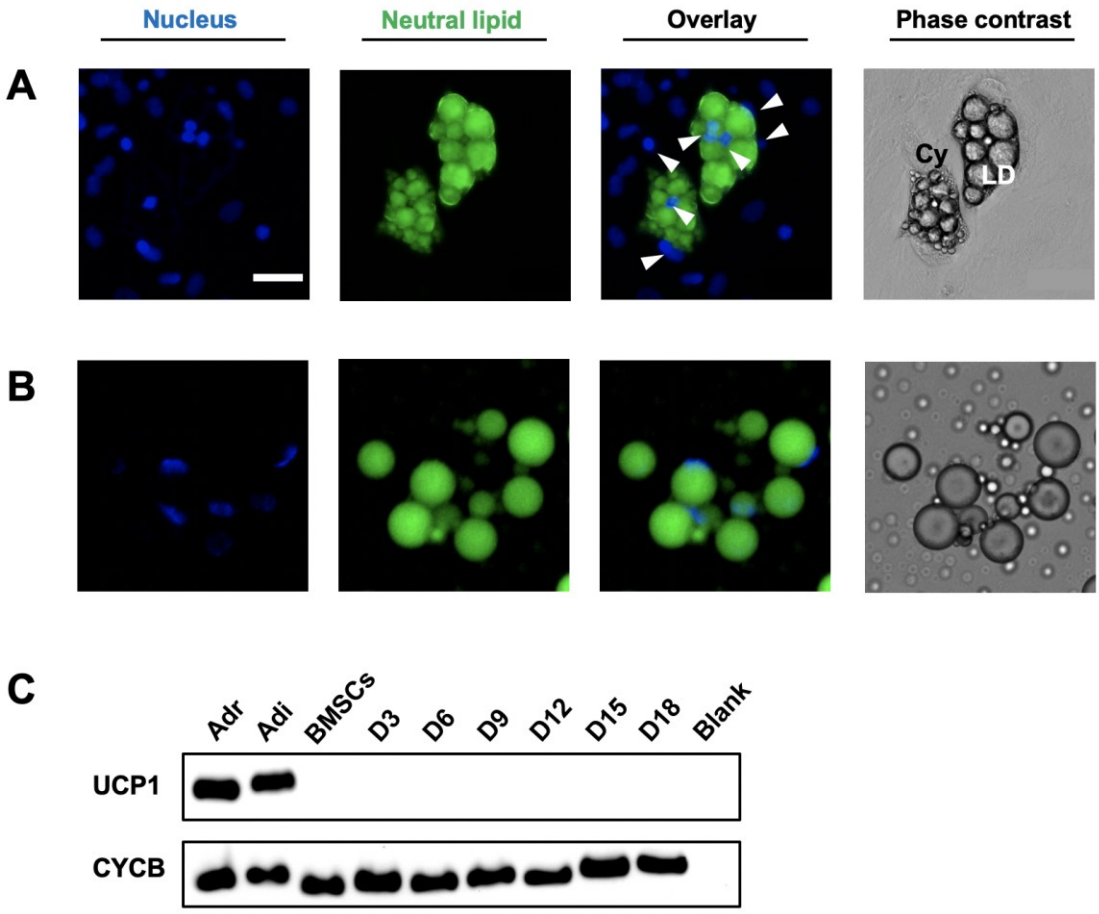

Figure 9. Adipocytes differentiated *in vitro* are morphologically distinct from BMAds *in vivo*. (A) Adipocytes differentiated from BMSCs *in vitro* are multinucleated (white arrowheads) and show a morphology of multilocular lipid droplets (LD) with a stretched cytoplasm (Cy). **(B)** Primary BMAds are unilocular and mononucleated in morphology. **(C)** Although resembling brown adipocytes in morphology, adipocytes differentiated *in vitro* are devoid of the classic thermogenic protein UCP1. Key: Adr, adrenal tissue; Adi, adipose tissue. Scale bar: 50 µm. Original agarose gel images can be found in **Appendix 3**.

4.3 Colour-based segmentation method as a tool to quantitate and describe BMAds from histological bone sections

To validate our semi-automated image analysis flow, we compared the number of BMAds counted manually and semi-automatically. We used five representative regions from histological bone sections (N= 4), resulting in twenty training images. The semi-automated quantitation method correlated strongly to the manual cell counts from both AdipoQuant- (r^2= 0.90, p<0.0001) and ImageJ- (r^2= 0.92, p<0.0001) based quantitation (**Fig. 10A and B)**. We then addressed some important differences between both image analysis flows, and how they affected the result. For instance, AdipoQuant false-positively detected empty spaces of the marrow vasculature or histological artefacts as BMAds (**Fig. 10C**). To note, we did not change the original script, except for the changeable parameters such as the size and circularity exclusion. To minimise false-positive detection, we developed our own detection script using ImageJ.

We aimed to improve the quantitation by ignoring false-positive detection from within the empty spaces using a morphological operator 'opening'. **Figure 10D** shows the improvement of this model when compared to the native AdipoQuant detection **(Fig. 10C)**. However, we did not find any statistically significant differences in the final BMAds quantitation between the two methods (data not shown). However, both methods failed to handle bad quality regions, such as staining precipitates and merged cells, among others. For instance, four BMAds were undetected due to the presence of a staining precipitate on top of the cells (**Fig. 10E**). On the other hand, three BMAds that merged into one cluster were not detected by both methods (**Fig 10F**). We initially thought that blurry images might affect the algorithm in the segmentation process and, therefore, the quantitation. To that end, the sections were rescanned with a multi-layer scan method comprising a 17 z-stack image with a 0.30 µm distance between stacks. We compared the error detection rate (**equation 4**) between the original and new image set with AdipoQuant and ImageJ. However, we did not detect a statistically significant difference in the error detection rate between different quality images (**Fig. 11**), suggesting that image quality is not the determiner for accurate detection of BMAds. On average, both semi-automated quantitation methods have an 18% error detection rate, regardless of image quality.

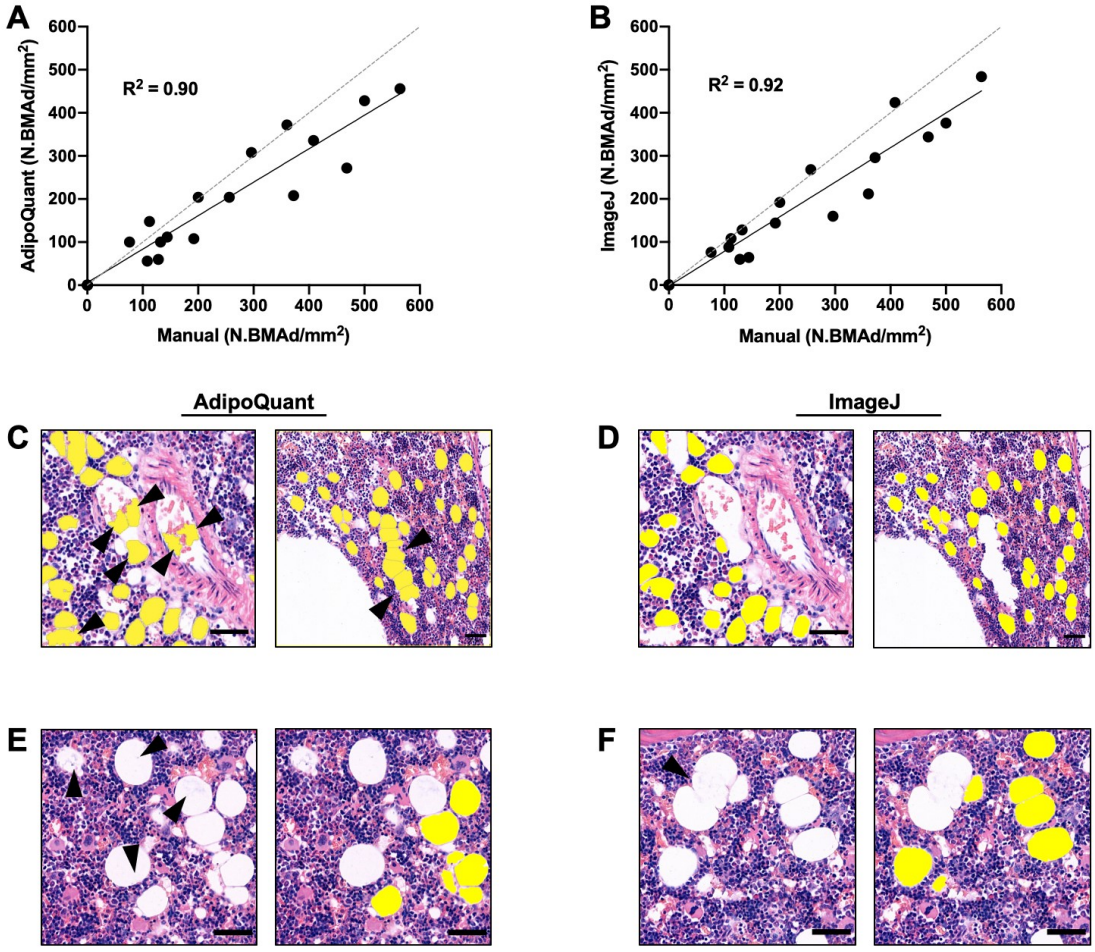

Figure 10. Validation of semi-automated BMAd quantitation methods from histological bone sections. The correlation analysis between manual and **(A)** AdipoQuant- or **(B)** ImageJ- based BMAd quantitation (N=20). Dotted lines represent an identity function. **(C)** Shown by black arrowheads, AdipoQuant false-positively detected BMAds within the bone marrow vasculature (left) and histological artefact region (right). **(D)** The morphological operator 'opening' consistently ignored possible error detections in non-BMAd area. Histological artefacts, such as the **(E)** staining precipitates or **(F)** broken BMAd membranes (black arrowheads) interfered with the effective segmentation by both quantitation methods Scale bars: 50 μm. Yellow circles represent detected BMAds.

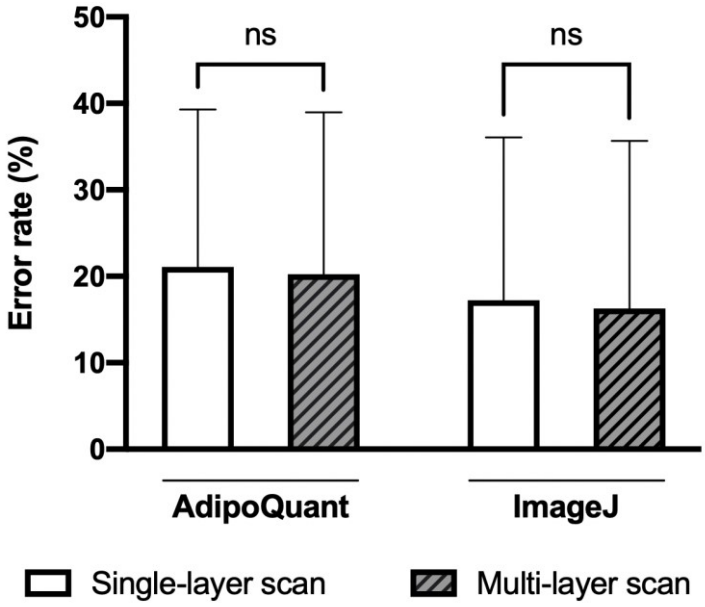

Figure 11. Image quality does not affect the quantitation regardless of image analysis methods. N= 20 per set; ns= not significant.

Lastly, we analysed the morphology of BMAds from our *ex vivo* imaging setup. On average, most of the BMAds detected were up to 1000 μm^2 in size (**Fig. 12A**). The median (Q1 – Q3) size of BMAds was 535.19 (361.40 – 792.30) μm^2. Interestingly, we found a regional trend of BMAd average size in the tibia. BMAds located in the diaphysis were significantly smaller than the distal epiphysis ($p< 0.0001$; **Fig. 12B**). **Figure 12C** shows the size distribution of BMAds from the respective regions. The median (Q1 – Q3) size of BMAds in the diaphysis and distal epiphysis was 503.30 (348.75 – 696.80) and 751.75 (439.32 – 1093.80) μm^2, respectively. Descriptively, BMAds in the diaphysis region were dispersed throughout the BM microenvironment, as opposed to the distal epiphysis region, where BMAds were tightly packed. Morphologically, marrow BMAds were more circular compared to the elongated shape of BMAds found in the distal part (**Fig. 12D**).

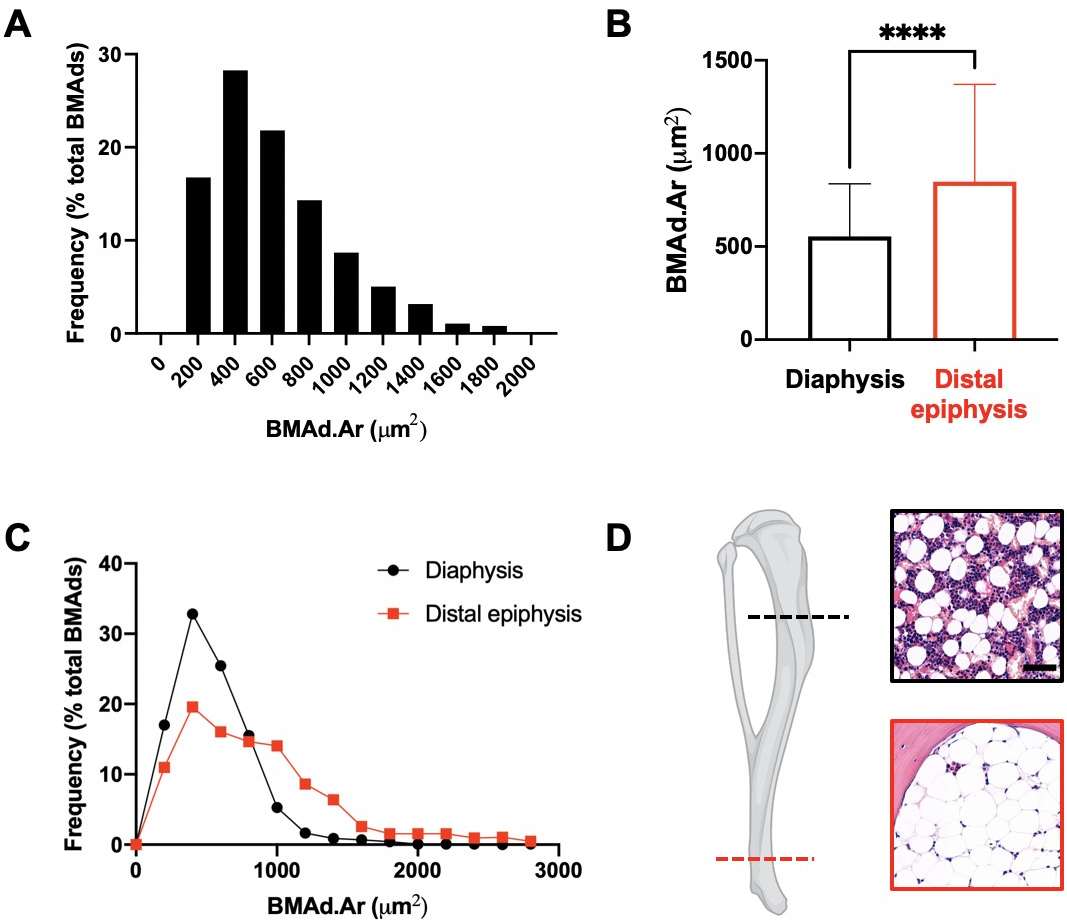

Figure 12. Morphological description of BMAds from *ex vivo* imaging. (A) Size distribution of BMAds from representative images (N= 20). **(B)** The average size of BMAds in the diaphysis and distal epiphysis region. **(C)** Size distribution of BMAds from regions from **(B)**. **(D)** Representative images of the diaphysis (black box) and distal epiphysis (Red box) region. Scale bar: 50 μm. Sizes of BMAds were analysed with ImageJ. The tibia illustration was created by Biorender (Biorender, Canada).

CHAPTER V
DISCUSSION

In this study, we evaluated the adipogenic differentiation model *in vitro* through gene expression and morphological analysis. To facilitate this aim, we first designed and evaluated the primers targeting adipocyte-specific mRNAs. We followed the recently published methodological guideline and grouped these primers as early (PPARG and CEBPA) and late (ADIPOQ and FABP4) adipocyte-specific markers (Tratwal et al., 2020b). We excluded the cytoskeletal reference gene ACTB, because it was not uniformly expressed during adipocyte differentiation (**Appendix 4**). This is likely due to the dynamic rearrangements of actin (Chen et al., 2018; Khan et al., 2020; Santos et al., 2016). Based on this notion, the use of a cytoskeletal marker as a housekeeping gene should be carefully evaluated. To that end, we selected cyclophilin B (CYCB, encoded by peptidyl-prolyl cis-trans isomerase B), an enzyme that catalyses the protein folding (Price et al., 1991), as our reference gene. Assessment of RT-qPCR cycle threshold value of CYCB revealed a stable expression level in both proliferation and differentiation state, and has been previously used to normalise gene expression in peripheral blood (Pachot et al., 2004) and breast tumour (Verjat et al., 2004) samples. For the first time, we reported the suitability of CYCB as a housekeeping gene to normalise the expression of adipocyte-specific rat mRNA expression *in vitro*.

Next, we tested the effect of different isolation methods of BMSCs on adipogenesis *in vitro.* Our results indicated that adipocyte-specific mRNAs were significantly upregulated in BMSCs obtained by the centrifugation method compared to the flush method (**Fig. 7A**). BM extraction by centrifugation allows minimal damage to the BM cells and a thorough extraction compared to the flushing technique (Dobson et al., 1999; Holt et al., 2014; Kelly et al., 2014). Incomplete extraction of the BM cells may reduce the heterogeneity of the BMSC population *in vitro*, which may affect the differentiation capability (reviewed in Tencerova and Kassem (2016)). We believe that the pro-adipogenic BMSCs, such as the Sca1- (Ambrosi et al., 2017), leptin receptor- (Yue et al., 2016) and RANKL-positive (Holt et al., 2014) populations, among others, may have remained in the BM cavity or damaged during the flushing process. Cell sorting by flow-cytometry would justify the BMSCs population contained from these BM isolates, which was not performed in this study. Nevertheless, we recommend the centrifugation method

as a simple and reproducible way to obtain BMSCs for various downstream applications. With this method, we were able to induce both adipogenesis and osteoblastogenesis (not shown) *in vitro*.

Interestingly, our results showed an opposing trend between the adipocyte-specific mRNA expression and morphology *in vitro* (**Fig. 7A-C**). This is in contrast to the common guideline that shows the morphological evidence of adipogenesis *in vitro* in the presence of IBMX (Tratwal et al., 2020b). To this discrepancy, we evaluated the effect of the solvent DMSO (**Appendix 5**). Of note, our DMSO concentration (0.05%) was lower than the previously suggested threshold of toxicity at 1% (Dludla et al., 2018) and a complete adipogenesis inhibition at 2% (Wang and Scott, 1993). However, they employed the 3T3-L1 cell line, as opposed to the primary cells used in this study. We observed the presence of adipocytes *in vitro* in our vehicle control group (IBMX- DMSO+; **Fig. 7C and F**), but not in the test group (IBMX+ DMSO+; **Fig. 7B and E**). This suggests that the presence of 0.05% DMSO did not restrict adipogenesis, as shown by morphology and mRNA expression analysis. Therefore, we believe that the combination of IBMX and DMSO produces multifactorial antagonistic effects on the adipocyte-specific phenotype regulator. For instance, perilipin, a surface marker protein, is essential for the formation of the lipid droplets (Itabe et al., 2017; Tang and Lane, 2012). The ablation of perilipin showed a lean and smaller adipocytes phenotype (Tansey et al., 2001). On this basis, we believe that a lipidomic study is required to accurately pinpoint the pathway disturbed by IBMX and DMSO. Alternatively, we strongly recommend dissolving IBMX in another solvent and carefully evaluate the effect of that solvent *in vitro*. Nevertheless, we excluded IBMX from our adipogenic cocktail, which is in line with the suggestion from Scott and colleagues (2011). Although induction cocktails can vary between laboratories, we suggest a solid optimisation to proceed before the actual analysis. At present, our adipogenic cocktail includes 10 µg/mL insulin and 10^{-6} M dexamethasone.

With the optimised adipogenesis protocol, we evaluated the temporal changes in the adipocyte-specific mRNA expression *in vitro* (**Fig. 8A**). Compared to the undifferentiated control, our adipogenic model confirmed a bona fide adipogenesis. The expression of the transcription factors mRNA was significantly higher than the control on day 15 of differentiation. This was later than expected. However, adipogenesis induction occurs in two phases (Lefterova et al., 2014), to which we only analysed the later phase. We did

not analyse other isoforms of PPARG and CEBPA, which may have been robustly present, but left undetected (Zhao et al., 2015). Besides, it is also possible that some BMSCs had committed to the adipogenic lineage before the induction and, therefore, expressed those factors. Hence, the BMSCs had set a higher threshold for the baseline expression level, which masked the major changes in the expression level analysed from the later time points. The mRNA expression of ADIPOQ and FABP4 was increasing during differentiation, and matched to the growing lipid droplet size (**Fig. 8B**). We could not observe a point to which these expressions peaked, but it is highly likely that if we had continued the culture, we might have been able to see these expression peaks.

The multilocular morphology of the adipocytes differentiated *in vitro* (**Fig. 9A**) has been reported in other studies, and is regarded as true BMAds (Tratwal et al., 2020b). In contrast, BMAds isolated from a 19-week-old SD rat were unilocular in morphology (**Fig. 9B**). However, it is likely that the completion of adipocyte maturation would ultimately form a unilocular adipocyte. This assumption is in line with the literature, confirming the presence of multilocular BMAds *in vivo* at 3-week-old (Craft et al., 2019), or in response to beta-adrenergic signalling at 12-week-old (Scheller et al., 2019). Without a specific staining method, it is difficult to histologically confirm multilocular BMAds *ex vivo*. From our HE stained histological bone sections (19-week-old rat), we were not confident to distinguish multilocular BMAds apart from small marrow spaces or other structures (not shown). In this study, the majority of BMAds *ex vivo* was unilocular in morphology.

Estimating adiposity *in vitro* has been a challenge in most studies. At present, measuring the absorbance of ORO eluates is a gold standard to semi-quantitatively estimate adiposity *in vitro* (Kraus et al., 2016; Mehlem et al., 2013). However, we noticed non-specific binding and staining precipitate of ORO on the plastic surface, which can affect the reading. Of note, we followed the recommendation from Mehlem and colleagues (2013) to freshly prepare ORO solution and a direct image acquisition without success. To that end, a cell-based quantitation is now preferred to analyse adipogenesis *in vitro* (Deutsch et al., 2014; Eggerschwiler et al., 2019; Yuan et al., 2019). We were able to develop our own ImageJ-based image analysis workflow to quantitate the adiposity *in vitro* by measuring the ORO area. Further, we optimised this design by excluding the empty area of the plastic surface to reflect a true biological adiposity fraction. To achieve this, we counterstained the other cells with a simple haematoxylin staining and extracted the area as a 'biological' area. By taking the ratio of ORO area to all detected area (ORO

and biological area), we reported an improved method in estimating the area-based adiposity by excluding the non-biological area (**Fig. 7D**).

It has been shown previously that BMSCs downregulate their proliferation rate upon adipogenic induction (Hung et al., 2004; Marcon et al., 2019). Morphologically, the nucleus of an adipocyte is located eccentrically. Based on these facts, we developed an additional parameter to report the proportion of adipocytes formed *in vitro* (**Fig. 7G**). Using a fluorescence imaging, we double-stained the nucleus and lipid droplet. From the image analysis workflow, we expanded the lipid area to artificially co-localise juxtaposed nuclei and consider the area as adipocyte clusters. However, it is important to note that the detected nuclei would not fully represent BMSCs due to the heterogeneity of the extracted BM cells, such as fibroblasts and osteoblasts. Also, we were able to reproduce a better area-based adiposity estimation *in vitro* by excluding the nuclear quantitation (data not shown). The fluorescent-based imaging offers high specificity for detection and analysis. For instance, we did not find any staining precipitates or non-specific binding, compared to the water-based method. The specific wavelength range allows better separation between two fluorophores compared to the overlapping colour spectrum from ORO and haematoxylin. In the future, we would recommend fluorophore-based imaging for a better quantitation method and a wider research application, such as live-cell imaging (**Fig. 8B**).

We were able to develop a simple and reproducible semi-automated BMAd quantitation from histological bone sections. However, some limitations of our image analysis method need to be addressed. First, we noticed that both AdipoQuant- and ImageJ-based workflow underestimated the counts compared to the manual approach (**Fig. 10A and B**). In this study, we reversely classified coloured pixels (cells and mineralised bones) as background, and the white-coloured pixels as foreground (BMAds). The algorithm segmented multiple broken adipocytes as one foreground object and increased the area. Secondly, other non-specific objects on top of the BMAd was segmented as background objects, which reduced the circularity of the suspected BMAd object. Based on the size and circularity exclusion parameter, these objects were not counted and, therefore, reduced the total quantitation. In addition, we noticed some out-of-focus regions in our section, which may have affected the quantitation. After rescanning the sections with a multi-focus mode (not shown), we did not find any significant differences in the quantitation (**Fig. 11**). Hence, we believe that the section quality is important for a better

detection, rather than the image quality. Also, the multi-focus scans are more than fifty times larger in size than the originals, making it impractical for a large-scale study. Ultimately, the discrete presence of the background colour of the 'ghost adipocyte' is a prerequisite for the algorithm to work optimally.

We developed our own image analysis workflow due to several reasons. First, although AdipoQuant had an acceptable rate in quantitating BMAds, we noticed a consistent false-positive detection, especially in the vascular or empty region, despite stricter size and circularity exclusion criteria. It is possible to adjust the native script to resolve this, but we intend to keep the workflow simple and reproducible for other users. Further, AdipoQuant allows the user to annotate exclusion regions for the analysis, which would resolve the limitation (Tratwal et al., 2020a). However, manually annotating these regions would defeat the purpose of automation in the digital image analysis. Secondly, we noticed that the watershed command in the AdipoQuant script at line #182 over-fragmented the adipocytes in an attempt to separate merged adipocyte objects. We had to exclude this step in this study to proceed with the quantitation method. Nevertheless, the quantitation by AdipoQuant has facilitated the quantitation of BMAds in a simple and reliable way. The full feature of MarrowQuant allowed us to also estimate mineralised bone and haematopoietic area (**Fig. 5A**), to which our workflow failed to discriminate.

To solve these two issues, we incorporated a third-party plugin MorphoLibJ (https://imagej.net/MorphoLibJ) into our script as a tool to minimise false-positive detection within these empty spaces. The morphological operator 'opening' took the coloured pixel, most commonly the erythrocytes, and eroded these pixels with a user-defined filter size. This was then followed by a pixel dilation with the same filter size to the image. As a result, the operation damaged the vessel area and, therefore, detection in this region was not possible due to the exclusion criteria (**Fig. 5B**). Similar to the AdipoQuant, however, the addition of the morphological operator failed to detect BMAd with objects on top of it. We did not perform watershed to separate touching objects due to the over-fragmentation issue, leading to multiple small but incorrect detections. Hence, adipocytes which were connected or covered by other objects, were left undetected regardless of the image analysis method.

Taken together, while HE stained histological sections remain a versatile method to assess BM adiposity, we would recommend immunostaining over water-based histological

staining. By specifically targeting adipocyte-specific membrane or cytoplasmic protein, we are confident that the error rate in BMAd detection would be minimal. For instance, immunostaining of perilipin, an adipocyte-specific surface marker, has been widely reported across literature to quantitate BMAds from histological bone sections (Ambrosi et al., 2017; Craft et al., 2019; Strissel et al., 2007; Zhou et al., 2017). Further, discrimination between BMAd, blood vessel and nerve fibre can be achieved by co-staining with the respective markers.

In this study, we extracted the descriptive information of BMAds from our image analysis workflow to report the area (Ad.Ar) and density (N.Ad/Ma.Ar) of BMAds. However, reporting these parameters must be carefully considered for the following reasons. First, BMAds exist in a 3D configuration *in vivo*, while we only analysed in the 2D perspective. By taking the largest BMAd that we detected as an area of a circle, we would redetect the same cell from twelve consecutive sections with varying sizes. Therefore, trimming each section apart by a roughly 50 µm distance would help in correctly analysing BMAd from 2D histological sections. This is especially important, as the expansion of BM adiposity is asymmetric especially during the development (Scheller et al., 2015). Secondly, reporting the number or size of BMAds should match the research question. For instance, a lipolytic assessment of BMAds would correlate better if the data is reported based on the size, not the number. In agreement with the working guideline, the number and size of BMAd reflect changes in adipogenesis and metabolic activity, respectively (Tratwal et al., 2020b).

Our results showed that, on average, the size of BMAds from a 19-week-old SD rat is similar to other rodent species, including the C57BL/6J and C3H/HeJ mice (Scheller et al., 2015; Scheller et al., 2019), but smaller than New Zealand white rabbits (Cawthorn et al., 2016) and humans (Attane et al., 2020). In line with Scheller's study on the regional characteristic of BMAds, we came to the same findings on the morphological differences of tibial BMAd size in the diaphysis and distal epiphysis region (Scheller et al., 2015). Descriptively, we observed that BMAds at the mid-diaphysis region (termed rMAT) were loosely interspersed within the marrow cavity to other BM cell populations. Contrastingly, BMAds found in the distal epiphysis region (termed cMAT) were tightly oriented. Morphologically, BMAd size in the cMAT is significantly larger and less circular compared to the rMAT (**Fig. 12B**). However, it is still preliminary to conclude the regional distinction of BMAds from this observation. More studies are needed to

functionally assess these descriptively distinct adipocyte populations within the bone marrow.

Although we were able to induce and characterise adipogenesis *in vitro*, the present study is limited to one induction protocol. We did not assess the effect of other induction compounds on adipogenesis *in vitro*, such as rosilgatizone or indomethacin, which may have increased adipogenesis to reflect *in vivo* BM adiposity. Secondly, we did not characterise the extracted BMSCs, despite the heterogeneous population of BMSCs has been well documented (Rennerfeldt et al., 2019; Whitfield et al., 2013). Regardless, we maintained the heterogeneity in our adipogenic culture to reflect *in vivo* condition. We have shown that the BMSCs were able to differentiate into osteoblast in a separate experiment, suggesting the multi-potential character of the isolated BMSCs. Finally, our ImageJ workflow was unable to discriminate the mineralised bone and haematopoietic area. We were not able to express the true marrow adiposity (%) based on this limitation, but the workflow allowed for better true-positive detections compared to the MarrowQuant. Nevertheless, the preference of the quantitation methods should be addressed accordingly.

In the future, more optimisation towards adipogenesis *in vitro* is of great importance. Isolated primary BMAds could be used as a baseline comparator for future comparative studies. Although we were able to extract primary BMAds, methodological work in isolating and purifying this population for the downstream application is ongoing. Long term, the comparative study would justify the suitability of the differentiation model as an alternative to primary BMAds. Ultimately, this may direct further optimisation of the preferred model for the BM adiposity research. Also, characterising BMSCs descriptively (surface markers) and functionally (trilineage differentiation) would be a natural step in the future. From the histological study, improvements in sample handling and staining that allows the preservation of BMAd integrity *ex vivo* are necessary, and may reduce nonspecific detections.

CHAPTER VI
CONCLUSION

In this study, we developed a simple model for adipocyte differentiation from BMSCs *in vitro* as a potential working application for bone marrow adiposity research. Our morphological and mRNA expression analysis confirmed adipogenesis *in vitro.* The comparability of our *in vitro* model to the primary BMAds remains to be investigated. In perspective, these models would provide an establishment towards a standard model in understanding BMAds. Further, we developed semi-automated image analysis methods to quantitate BMAds from our *in* vitro model and histological bone sections based on the colour principle. We reported an improved adiposity estimation and an estimation of the proportion of adipocytes formation *in vitro*. From the histological study, our quantitation method could discriminate similar non-BMAds objects, such as blood vessels and empty marrow spaces, and is comparable to manual quantitation. At present, the efficiency of the estimation is determined by section quality, to which careful sample preparation and section handling are essential to preserve BMAds morphology *ex vivo* for accurate detection. Future developments to address this issue are required, especially in the direction of immunostaining-based quantitation.

ACKNOWLEDGEMENTS

I would like to express my gratitude to Adj. Prof. Kaisa Ivaska for her continuous support and guidance to make this research possible. I am extremely grateful for the opportunity to join a dynamic research group that she leads at the University of Turku.

I am also thankful for the practical guidance and suggestions from the group members Milja Arponen, Niki Jalava and Sana Rais.

I would like to acknowledge all the input I received from other research groups and laboratory personnel at the Institute of Biomedicine.

This thesis would not have been possible without the generous scholarship and study grants from Åbo Akademi University from the very beginning. I was able to pursue my interest in the field of bone biology and apply the knowledge that I learnt from the BIMA programme.

In this difficult time, I received endless motivation from my friends from all over the world, and for that, I am forever grateful.

Thank you to all of my friends in Finland for the amazing two years. I will never forget the joy that we shared when we saw the northern lights for the very first time.

Last but not least, this achievement goes to my family for their constant support throughout my study.

REFERENCES

Ambrosi, T.H., A. Scialdone, A. Graja, S. Gohlke, A.M. Jank, C. Bocian, L. Woelk, H. Fan, D.W. Logan, A. Schurmann, et al. 2017. Adipocyte Accumulation in the Bone Marrow during Obesity and Aging Impairs Stem Cell-Based Hematopoietic and Bone Regeneration. *Cell Stem Cell*. 20:771-784.

Attane, C., D. Esteve, K. Chaoui, J.S. Iacovoni, J. Corre, M. Moutahir, P. Valet, O. Schiltz, N. Reina, and C. Muller. 2020. Human Bone Marrow Is Comprised of Adipocytes with Specific Lipid Metabolism. *Cell Rep.* 30:949-958.

Bankhead, P., M.B. Loughrey, J.A. Fernandez, Y. Dombrowski, D.G. McArt, P.D. Dunne, S. McQuaid, R.T. Gray, L.J. Murray, H.G. Coleman, et al. 2017. QuPath: Open source software for digital pathology image analysis. *Sci. Rep.* 7:16878.

Blagosklonny, M.V., H.H. Zhang, J. Huang, K. Düvel, B. Boback, S. Wu, R.M. Squillace, C.-L. Wu, and B.D. Manning. 2009. Insulin Stimulates Adipogenesis through the Akt-TSC2-mTORC1 Pathway. *PLoS ONE*. 4:e6189.

Boroumand, P., and A. Klip. 2020. Bone marrow adipose cells – cellular interactions and changes with obesity. *J. Cell Sci*. 133.

Boxall, S.A., and E. Jones. 2012. Markers for characterization of bone marrow multipotential stromal cells. *Stem Cells Int*. 2012:975871.

Bravenboer, N., M.A. Bredella, C. Chauveau, A. Corsi, E. Douni, W.F. Ferris, M. Riminucci, P.G. Robey, S. Rojas-Sutterlin, C. Rosen, et al. 2019. Standardised Nomenclature, Abbreviations, and Units for the Study of Bone Marrow Adiposity: Report of the Nomenclature Working Group of the International Bone Marrow Adiposity Society. *Front. Endocrinol.* 10:923.

Bredella, M.A., P.K. Fazeli, K.K. Miller, M. Misra, M. Torriani, B.J. Thomas, R.H. Ghomi, C.J. Rosen, and A. Klibanski. 2009. Increased bone marrow fat in anorexia nervosa. *J. Clin. Endocrinol. Metab.* 94:2129-2136.

Calvi, L.M. 2020. Bone marrow and the hematopoietic stem cell niche. *In* Principles of Bone Biology. J.P. Bilezikian, T.J. Martin, T.L. Clemens, and C. Rosen, editors. Academic Press, Cambridge, MA. 73-87.

Cawthorn, W.P., E.L. Scheller, S.D. Parlee, H.A. Pham, B.S. Learman, C.M.H. Redshaw, R.J. Sulston, A.A. Burr, A.K. Das, B.R. Simon, et al. 2016. Expansion of Bone Marrow Adipose Tissue During Caloric Restriction Is Associated With Increased Circulating Glucocorticoids and Not With Hypoleptinemia. *Endocrinology*. 157:508-521.

Chen, L., H. Hu, W. Qiu, K. Shi, and M. Kassem. 2018. Actin depolymerization enhances adipogenic differentiation in human stromal stem cells. *Stem Cell Res.* 29:76-83.

Chen, Q., P. Shou, C. Zheng, M. Jiang, G. Cao, Q. Yang, J. Cao, N. Xie, T. Velletri, X. Zhang, et al. 2016. Fate decision of mesenchymal stem cells: adipocytes or osteoblasts? *Cell Death Differ*. 23:1128-1139.

Craft, C.S., H. Robles, M.R. Lorenz, E.D. Hilker, K.L. Magee, T.L. Andersen, W.P. Cawthorn, O.A. MacDougald, C.A. Harris, and E.L. Scheller. 2019. Bone marrow adipose tissue does not express UCP1 during development or adrenergic-induced remodeling. *Sci. Rep*. 9:17427.

David, V., A. Martin, M.H. Lafage-Proust, L. Malaval, S. Peyroche, D.B. Jones, L. Vico, and A. Guignandon. 2007. Mechanical loading down-regulates peroxisome proliferator-activated receptor gamma in bone marrow stromal cells and favors osteoblastogenesis at the expense of adipogenesis. *Endocrinology*. 148:2553-2562.

Deutsch, M.J., S.C. Schriever, A.A. Roscher, and R. Ensenauer. 2014. Digital image analysis approach for lipid droplet size quantitation of Oil Red O-stained cultured cells. *Anal. Biochem.* 445:87-89.

Dludla, P.V., B. Jack, A. Viraragavan, C. Pheiffer, R. Johnson, J. Louw, and C.J.F. Muller. 2018. A dose-dependent effect of dimethyl sulfoxide on lipid content, cell viability and oxidative stress in 3T3-L1 adipocytes. *Toxicol. Rep.* 5:1014-1020.

Dobson, K., L. Reading, M. Haberey, X. Marine, and A. Scutt. 1999. Centrifugal isolation of bone marrow from bone: an improved method for the recovery and quantitation of bone marrow osteoprogenitor cells from rat tibiae and femurae. *Calcif. Tissue Int.* 65:411-413.

Eggerschwiler, B., D.D. Canepa, H.C. Pape, E.A. Casanova, and P. Cinelli. 2019. Automated digital image quantification of histological staining for the analysis of the trilineage differentiation potential of mesenchymal stem cells. *Stem Cell Res. Ther.* 10:69.

Evans, A.L., M.A. Paggiosi, R. Eastell, and J.S. Walsh. 2015. Bone density, microstructure and strength in obese and normal weight men and women in younger and older adulthood. *J. Bone Miner. Res.* 30:920-928.

Fairfield, H., C. Falank, M. Farrell, C. Vary, J.M. Boucher, H. Driscoll, L. Liaw, C.J. Rosen, and M.R. Reagan. 2019. Development of a 3D bone marrow adipose tissue model. *Bone*. 118:77-88.

Fam, T.K., A.S. Klymchenko, and M. Collot. 2018. Recent Advances in Fluorescent Probes for Lipid Droplets. *Materials*. 11.

Fan, Y., J.I. Hanai, P.T. Le, R. Bi, D. Maridas, V. DeMambro, C.A. Figueroa, S. Kir, X. Zhou, M. Mannstadt, et al. 2017. Parathyroid Hormone Directs Bone Marrow Mesenchymal Cell Fate. *Cell Metab*. 25:661-672.

Fayyad, A., A. Khan, S. Abdallah, S. Alomran, K. Bajou, and M. Khattak. 2019. Rosiglitazone Enhances Browning Adipocytes in Association with MAPK and PI3-K Pathways During the Differentiation of Telomerase-Transformed Mesenchymal Stromal Cells into Adipocytes. *Int. J. Mol. Sci.* 20:1618.

Griffith, J.F., D.K. Yeung, H.T. Ma, J.C. Leung, T.C. Kwok, and P.C. Leung. 2012. Bone marrow fat content in the elderly: a reversal of sex difference seen in younger subjects. *J. Magn. Reson. Imaging*. 36:225-230.

Hardouin, P., T. Rharass, and S. Lucas. 2016. Bone Marrow Adipose Tissue: To Be or Not To Be a Typical Adipose Tissue? *Front. Endocrinol.* 7:85.

Holt, V., A.I. Caplan, and S.E. Haynesworth. 2014. Identification of a subpopulation of marrow MSC-derived medullary adipocytes that express osteoclast-regulating molecules: marrow adipocytes express osteoclast mediators. *PLoS One*. 9:e108920.

Huang, S., L. Xu, Y. Sun, T. Wu, K. Wang, and G. Li. 2015. An improved protocol for isolation and culture of mesenchymal stem cells from mouse bone marrow. *J. Orthop. Translat*. 3:26-33.

Hung, S.C., C.F. Chang, H.L. Ma, T.H. Chen, and L. Low-Tone Ho. 2004. Gene expression profiles of early adipogenesis in human mesenchymal stem cells. *Gene*. 340:141-150.

Itabe, H., T. Yamaguchi, S. Nimura, and N. Sasabe. 2017. Perilipins: a diversity of intracellular lipid droplet proteins. *Lipids Health Dis*. 16:83.

Kawai, M., F.J.A. de Paula, and C.J. Rosen. 2012. New insights into osteoporosis: the bone-fat connection. *J. Intern. Med.* 272:317-329.

Kelly, N.H., J.C. Schimenti, F. Patrick Ross, and M.C. van der Meulen. 2014. A method for isolating high quality RNA from mouse cortical and cancellous bone. *Bone*. 68:1-5.

Kenkre, J.S., and J. Bassett. 2018. The bone remodelling cycle. *Ann. Clin. Biochem.* 55:308-327.

Khan, A.U., R. Qu, T. Fan, J. Ouyang, and J. Dai. 2020. A glance on the role of actin in osteogenic and adipogenic differentiation of mesenchymal stem cells. *Stem Cell Res. Ther.* 11:283.

Kraus, N.A., F. Ehebauer, B. Zapp, B. Rudolphi, B.J. Kraus, and D. Kraus. 2016. Quantitative assessment of adipocyte differentiation in cell culture. *Adipocyte*. 5:351-358.

Lefterova, M.I., A.K. Haakonsson, M.A. Lazar, and S. Mandrup. 2014. PPARgamma and the global map of adipogenesis and beyond. *Trends Endocrinol. Metab.* 25:293-302.

Lewis, J.W., J.R. Edwards, A.J. Naylor, and H.M. McGettrick. 2021. Adiponectin signalling in bone homeostasis, with age and in disease. *Bone Res.* 9.

Li, J., N. Zhang, X. Huang, J. Xu, J.C. Fernandes, K. Dai, and X. Zhang. 2013. Dexamethasone shifts bone marrow stromal cells from osteoblasts to adipocytes by C/EBPalpha promoter methylation. *Cell Death Dis*. 4:e832.

Li, Q., Y. Wu, and N. Kang. 2018. Marrow Adipose Tissue: Its Origin, Function, and Regulation in Bone Remodeling and Regeneration. *Stem Cells Int*. 2018:7098456.

Li, Y., Y. Meng, and X. Yu. 2019. The Unique Metabolic Characteristics of Bone Marrow Adipose Tissue. *Front. Endocrinol.* 10:69.

Livak, K.J., and T.D. Schmittgen. 2001. Analysis of relative gene expression data using real-time quantitative PCR and the 2(-Delta Delta C(T)) Method. *Methods*. 25:402-408.

Marcon, B.H., P. Shigunov, L. Spangenberg, I.T. Pereira, A.M. de Aguiar, R. Amorín, C.K. Rebelatto, A. Correa, and B. Dallagiovanna. 2019. Cell cycle genes are downregulated after adipogenic triggering in human adipose tissue-derived stem cells by regulation of mRNA abundance. *Sci. Rep.* 9:5611.

Maridas, D.E., E. Rendina-Ruedy, P.T. Le, and C.J. Rosen. 2018. Isolation, Culture, and Differentiation of Bone Marrow Stromal Cells and Osteoclast Progenitors from Mice. *J. Vis. Exp.*:e56750.

Martin, P.J., N. Haren, O. Ghali, A. Clabaut, C. Chauveau, P. Hardouin, and O. Broux. 2015. Adipogenic RNAs are transferred in osteoblasts via bone marrow adipocytes-derived extracellular vesicles (EVs). *BMC Cell Biol*. 16:10.

Mattiucci, D., G. Maurizi, V. Izzi, L. Cenci, M. Ciarlantini, S. Mancini, E. Mensa, R. Pascarella, M. Vivarelli, A. Olivieri, et al. 2018. Bone marrow adipocytes support hematopoietic stem cell survival. *J. Cell Physiol.* 233:1500-1511.

McGrath, C., J.S. Sankaran, N. Misaghian-Xanthos, B. Sen, Z. Xie, M.A. Styner, X. Zong, J. Rubin, and M. Styner. 2020. Exercise Degrades Bone in Caloric Restriction, Despite Suppression of Marrow Adipose Tissue (MAT). *J. Bone Miner. Res.* 35:106-115.

Mehlem, A., C.E. Hagberg, L. Muhl, U. Eriksson, and A. Falkevall. 2013. Imaging of neutral lipids by oil red O for analyzing the metabolic status in health and disease. *Nat. Protoc.* 8:1149-1154.

Mistry, S.D., G.N. Woods, S. Sigurdsson, S.K. Ewing, T.F. Hue, G. Eiriksdottir, K. Xu, J.F. Hilton, D.M. Kado, V. Gudnason, et al. 2018. Sex hormones are negatively associated with vertebral bone marrow fat. *Bone*. 108:20-24.

Muruganandan, S., A.M. Ionescu, and C.J. Sinal. 2020. At the Crossroads of the Adipocyte and Osteoclast Differentiation Programs: Future Therapeutic Perspectives. *Int. J. Mol. Sci.* 21.

Napoli, N., M. Chandran, D.D. Pierroz, B. Abrahamsen, A.V. Schwartz, and S.L. Ferrari. 2016. Mechanisms of diabetes mellitus-induced bone fragility. *Nat. Rev. Endocrinol.* 13:208-219.

Pachot, A., J.L. Blond, B. Mougin, and P. Miossec. 2004. Peptidylpropyl isomerase B (PPIB): a suitable reference gene for mRNA quantification in peripheral whole blood. *J. Biotechnol.* 114:121-124.

Pagnotti, G.M., and M. Styner. 2016. Exercise Regulation of Marrow Adipose Tissue. *Front. Endocrinol.* 7:94.

Patel, V.S., M. Ete Chan, J. Rubin, and C.T. Rubin. 2018. Marrow Adiposity and Hematopoiesis in Aging and Obesity: Exercise as an Intervention. *Curr. Osteoporos. Rep.* 16:105-115.

Petridou, E., C.S. Mantzoros, N. Dessypris, S.K. Dikalioti, and D. Trichopoulos. 2006. Adiponectin in relation to childhood myeloblastic leukaemia. *Br. J. Cancer*. 94:156-160.

Pham, T.T., K.K. Ivaska, J.C. Hannukainen, K.A. Virtanen, M.E. Lidell, S. Enerbäck, K. Mäkelä, R. Parkkola, S. Piirola, V. Oikonen, et al. 2020. Human Bone Marrow Adipose Tissue is a Metabolically Active and Insulin-Sensitive Distinct Fat Depot. *J. Clin. Endocrinol. Metab.* 105:2300-2310.

Pollock, N., E. Laing, C. Baile, M. Hamrick, D. Hall, and R. Lewis. 2007. Is adiposity advantageous for bone strength? A peripheral quantitative computed tomography study in late adolescent females. *Am. J. Clin. Nutr.* 86:1530-1538.

Price, E., L. Zydowsky, M. Jin, C. Baker, F. McKeon, and C. Walsh. 1991. Human cyclophilin B: A second cyclophilin gene encodes a peptidyl-prolylisomerasewithasignalsequence. *Proc. Nat. Acad. Sci*. 88:1903-1907.

Qiang, G., H. Whang Kong, S. Xu, H.A. Pham, S.D. Parlee, A.A. Burr, V. Gil, J. Pang, A. Hughes, X. Gu, et al. 2016. Lipodystrophy and severe metabolic dysfunction in mice with adipose tissue-specific insulin receptor ablation. *Mol. Metab.* 5:480-490.

Rendina-Ruedy, E., and C.J. Rosen. 2020. Lipids in the Bone Marrow: An Evolving Perspective. *Cell Metab*. 31:219-231.

Rennerfeldt, D.A., J.S. Raminhos, S.M. Leff, P. Manning, and K.J. Van Vliet. 2019. Emergent heterogeneity in putative mesenchymal stem cell colonies: Single-cell time lapsed analysis. *PLoS One*. 14:e0213452.

Reseland, J., I. Bakke, G. Qvigstad, L. Eide, O. Hjertner, J. Gordeladze, and C. Drevon. 2001. Leptin Is Expressed in and Secreted from Primary Cultures of Human Osteoblasts and Promotes Bone Mineralization. *J. Bone Miner. Res.* 16:1426-1433.

Robling, A., and C. Turner. 2009. Mechanical Signaling for Bone Modeling and Remodeling. *Crit. Rev. Eukaryot. Gene Expr.* 19:319-338.

Rzonca, S.O., L.J. Suva, D. Gaddy, D.C. Montague, and B. Lecka-Czernik. 2004. Bone is a target for the antidiabetic compound rosiglitazone. *Endocrinology*. 145:401-406.

Santos, B.P., L.F. da Costa Diesel, L. da Silva Meirelles, N.B. Nardi, and M. Camassola. 2016. Identification of suitable reference genes for quantitative gene expression analysis in rat adipose stromal cells induced to trilineage differentiation. *Gene*. 594:211-219.

Scheller, E.L., C.R. Doucette, B.S. Learman, W.P. Cawthorn, S. Khandaker, B. Schell, B. Wu, S.-Y. Ding, M.A. Bredella, P.K. Fazeli, et al. 2015. Region-specific variation in the properties of skeletal adipocytes reveals regulated and constitutive marrow adipose tissues. *Nat. Commun.* 6:7808.

Scheller, E.L., S. Khandaker, B.S. Learman, W.P. Cawthorn, L.M. Anderson, H.A. Pham, H. Robles, Z. Wang, Z. Li, S.D. Parlee, et al. 2019. Bone marrow adipocytes resist lipolysis and remodeling in response to beta-adrenergic stimulation. *Bone*. 118:32-41.

Schindelin, J., I. Arganda-Carreras, E. Frise, V. Kaynig, M. Longair, T. Pietzsch, S. Preibisch, C. Rueden, S. Saalfeld, B. Schmid, et al. 2012. Fiji: an open-source platform for biological-image analysis. *Nat. Methods.* 9:676-682.

Scott, M.A., V.T. Nguyen, B. Levi, and A.W. James. 2011. Current Methods of Adipogenic Differentiation of Mesenchymal Stem Cells. *Stem Cells Dev.* 20:1793-1804.

Sebo, Z.L., E. Rendina-Ruedy, G.P. Ables, D.M. Lindskog, M.S. Rodeheffer, P.K. Fazeli, and M.C. Horowitz. 2019. Bone Marrow Adiposity: Basic and Clinical Implications. *Endocr. Rev.* 40:1187-1206.

Shen, W., J. Chen, M. Punyanitya, S. Shapses, S. Heshka, and S.B. Heymsfield. 2007. MRI-measured bone marrow adipose tissue is inversely related to DXA-measured bone mineral in Caucasian women. *Osteoporos. Int.* 18:641-647.

Singhal, V., and M.A. Bredella. 2019. Marrow adipose tissue imaging in humans. *Bone*. 118:69-76.

Strissel, K.J., Z. Stancheva, H. Miyoshi, J.W. Perfield, J. DeFuria, Z. Jick, A.S. Greenberg, and M.S. Obin. 2007. Adipocyte Death, Adipose Tissue Remodeling, and Obesity Complications. *Diabetes*. 56:2910-2918.

Styner, M., G.M. Pagnotti, C. McGrath, X. Wu, B. Sen, G. Uzer, Z. Xie, X. Zong, M.A. Styner, C.T. Rubin, et al. 2017. Exercise Decreases Marrow Adipose Tissue Through ss-Oxidation in Obese Running Mice. *J. Bone Miner. Res.* 32:1692-1702.

Suchacki, K.J., A.A.S. Tavares, D. Mattiucci, E.L. Scheller, G. Papanastasiou, C. Gray, M.C. Sinton, L.E. Ramage, W.A. McDougald, A. Lovdel, et al. 2020. Bone marrow adipose tissue is a unique adipose subtype with distinct roles in glucose homeostasis. *Nat. Commun.* 11:3097.

Syed, F.A., M.J. Oursler, T.E. Hefferanm, J.M. Peterson, B.L. Riggs, and S. Khosla. 2008. Effects of estrogen therapy on bone marrow adipocytes in postmenopausal osteoporotic women. *Osteoporos Int*. 19:1323-1330.

Tang, Q.Q., and M.D. Lane. 2012. Adipogenesis: From Stem Cell to Adipocyte. *Annu. Rev. Biochem.* 81:715-736.

Tansey, J.T., C. Sztalryd, J. Gruia-Gray, D.L. Roush, J.V. Zee, O. Gavrilova, M.L. Reitman, C.X. Deng, C. Li, A.R. Kimmel, et al. 2001. Perilipin ablation results in a lean mouse with aberrant adipocyte lipolysis, enhanced leptin production, and resistance to diet-induced obesity. *Proc. Natl. Acad. Sci. U.S.A.* 98:6494-6499.

Tencerova, M., F. Figeac, N. Ditzel, H. Taipaleenmäki, T.K. Nielsen, and M. Kassem. 2018. High-Fat Diet-Induced Obesity Promotes Expansion of Bone Marrow Adipose Tissue and Impairs Skeletal Stem Cell Functions in Mice. *J. Bone Miner. Res.* 33:1154-1165.

Tencerova, M., and M. Kassem. 2016. The Bone Marrow-Derived Stromal Cells: Commitment and Regulation of Adipogenesis. *Front. Endocrinol.* 7:127.

Toneatto, J., N.L. Charó, A. Naselli, M. Muñoz-Bernart, A. Lombardi, and G. Piwien-Pilipuk. 2014. Corticosteroid Receptors, Their Chaperones and Cochaperones: How Do They Modulate Adipogenesis? *Nuclear Receptor Research*. 1:101092.

Tratwal, J., D. Bekri, C. Boussema, R. Sarkis, N. Kunz, T. Koliqi, S. Rojas-Sutterlin, F. Schyrr, D.N. Tavakol, V. Campos, et al. 2020a. MarrowQuant Across Aging and Aplasia: A Digital Pathology Workflow for Quantification of Bone Marrow Compartments in Histological Sections. *Front. Endocrinol.* 11:480.

Tratwal, J., R. Labella, N. Bravenboer, G. Kerckhofs, E. Douni, E.L. Scheller, S. Badr, D.C. Karampinos, S. Beck-Cormier, B. Palmisano, et al. 2020b. Reporting Guidelines, Review of Methodological Standards, and Challenges Toward Harmonization in Bone Marrow Adiposity Research. Report of the Methodologies Working Group of the International Bone Marrow Adiposity Society. *Front. Endocrinol.* 11:65.

Verjat, T., E. Cerrato, M. Jacobs, P. Leissner, and B. Mougin. 2004. Multiparametric duplex real-time nucleic acid sequence-based amplification assay for mRNA profiling. *Biotechniques*. 37:476-481.

Wang, H., and R.E. Scott. 1993. Inhibition of distinct steps in the adipocyte differentiation pathway in 3T3 T mesenchymal stem cells by dimethyl sulphoxide (DMSO). *Cell Prolif.* 26:55-66.

Whitfield, M.J., W.C. Lee, and K.J. Van Vliet. 2013. Onset of heterogeneity in culture-expanded bone marrow stromal cells. *Stem Cell Res*. 11:1365-1377.

Yang, D.C., H.J. Tsay, S.Y. Lin, S.H. Chiou, M.J. Li, T.J. Chang, and S.C. Hung. 2008. cAMP/PKA regulates osteogenesis, adipogenesis and ratio of RANKL/OPG mRNA expression in mesenchymal stem cells by suppressing leptin. *PLoS One*. 3:e1540.

Yokota, T., C.S. Meka, T. Kouro, K.L. Medina, H. Igarashi, M. Takahashi, K. Oritani, T. Funahashi, Y. Tomiyama, Y. Matsuzawa, et al. 2003. Adiponectin, a fat cell product, influences the earliest lymphocyte precursors in bone marrow cultures by activation of the cyclooxygenase-prostaglandin pathway in stromal cells. *J Immunol*. 171:5091-5099.

Yuan, C., S. Chakraborty, K.K. Chitta, S. Subramanian, T.E. Lim, W. Han, K.N. Bhanu Prakash, and S. Sugii. 2019. Fast Adipogenesis Tracking System (FATS)-a robust, high-throughput, automation-ready adipogenesis quantification technique. *Stem Cell Res. Ther.* 10:38.

Yue, R., B.O. Zhou, I.S. Shimada, Z. Zhao, and S.J. Morrison. 2016. Leptin Receptor Promotes Adipogenesis and Reduces Osteogenesis by Regulating Mesenchymal Stromal Cells in Adult Bone Marrow. *Cell Stem Cell*. 18:782-796.

Zhang, H., S. Kumar, A. Barnett, and M. Eggo. 2000. Ceiling culture of mature human adipocytes: use in studies of adipocyte functions. *J Endocrinol*. 164:119-128.

Zhao, X.Y., X.Y. Chen, Z.J. Zhang, Y. Kang, W.M. Liao, W.H. Yu, and A.P. Xiang. 2015. Expression patterns of transcription factor PPARgamma and C/EBP family members during in vitro adipogenesis of human bone marrow mesenchymal stem cells. *Cell Biol. Int.* 39:457-465.

Zhou, B.O., H. Yu, R. Yue, Z. Zhao, J.J. Rios, O. Naveiras, and S.J. Morrison. 2017. Bone marrow adipocytes promote the regeneration of stem cells and haematopoiesis by secreting SCF. *Nat. Cell Biol.* 19:891-903.

APPENDICES

APPENDIX – 1: SCRIPT FOR ADIPOCYTES QUANTITATION *IN VITRO*

The following scripts were written in IJ1 Macro language native to the ImageJ version 2.1.0 and contain two parts. The first part of the script extracts the total haematoxylin and oil-red-O area to express adiposity *in vitro*. The second script extracts the number of detected nucleus and lipid droplets from segmented objects from the DAPI (447/60 nm) and GFP channel (525/50 nm), respectively (Invitrogen, USA). For simplicity, the batch analysis command was excluded, displaying only the core command to facilitate these aims. Lines containing changeable parameters are shown in red fonts. Different microscope setups may result in different analysis result, especially in the scaling factor.

Part 1 – Colour-based segmentation to quantitate adiposity area (%) *in vitro*

```
title = getTitle();
selectImage(title);
run("Colour Deconvolution", "vectors=[H AEC]");
close();
//Analysing BMAd picture
rename("BMAd");
setAutoThreshold("Default");
//run("Threshold...");
setThreshold(0, 100);
//setThreshold(0, 100);
setOption("BlackBackground", true);
run("Convert to Mask");
run("Analyze Particles...", "size=500-Infinity display clear summarize add");
//Analysing BMSC picture
selectWindow(title+"-(Colour_1)");
rename("BMSC");
setThreshold(0, 232);
//setThreshold(0, 232);
setOption("BlackBackground", true);
run("Convert to Mask");
run("Analyze Particles...", "size=500-Infinity display clear summarize add");
close("Results");
selectWindow("Summary");
Table.rename("Summary", "Results");
String.copyResults();
```

Part 2 – Co-localisation based counting to express adipogenesis (%) *in vitro*

```
1. run("Options...", "iterations=1 count=1 black");
2. //Scaling factors - Always enter the correct size of the images depending
   on microscope models
3. run("Set Scale...", "distance=2048 known=853.2992 unit=um");
4. //Pre-processing
5. title = getTitle();
6. run("Split Channels");
7. selectWindow(title+" (red)");
8. close();
9. //Segmenting nuclei
10. selectWindow(title+" (blue)");
11. setAutoThreshold("Default dark");
12. //run("Threshold...");
13. //setThreshold(43, 255);
14. run("Convert to Mask");
15. run("Watershed");
16. //Quantitating the amount of nuclei
17. run("Analyze Particles...", "size=50-Infinity circularity=0.30-1.00
   display exclude clear summarize add");
18. //Segmenting lipid droplets and merge into one defined cell
19. selectWindow(title+" (green)");
20. setAutoThreshold("Default dark");
21. //run("Threshold...");
22. //setThreshold(54, 255);
23. run("Convert to Mask");
24. run("Morphological Filters", "operation=dilation element=Disk
   radius=10");
25. rename("Dilated nuclei");
26. //Superimposing segmented adipocytes and nuclei, and take the overlapping
   nuclei as double positive counts
27. imageCalculator("AND create", title+" (blue)","Dilated nuclei");
28. rename("Double positives count");
29. //Count double positives cells
30. run("Analyze Particles...", "size=50-Infinity circularity=[0 -1.00]
   display exclude clear summarize add");
31. selectWindow("Summary");
32. Table.rename("Summary", "Results");
33. String.copyResults();
```

APPENDIX – 2: SCRIPT FOR BMADS QUANTITATION *EX VIVO*

The following script describes the command used to quantitate BMAds from *ex vivo* histological bone sections stained with haematoxylin and eosin. Briefly, delipidation during alcohol treatment resulted in an empty singular and rather circular structure of BMAd within the enclosed and stained membrane. This empty structure has similar pixel values to the background colour which is used as a principle of the detection. We optimised it further to ignore non-specific detection like small blood vessels by sequentially eroded and dilated small detected objects within the falsely-presumed BMAd. Lastly, we filtered our segmented objects with a size filter to detect BMAds and expressed the results as the total number and shape parameter of BMAd within the analysed region. Different microscope setup may affect the quantitation, especially in the scaling factors and segmentation threshold value. Changeable parameters are shown in red fonts.

```
1. //Preprocessing
2. run("Set Scale...", "distance=2063 known=500.35 pixel=1.000 unit=µm");
3. // This helps to maintain ImageJ hierarchy on differently titled images
4. run("Duplicate...", "title=Annotated");
5. run("Duplicate...", "title=original");
6. run("8-bit");
7. setAutoThreshold("Default dark");
8. //run("Threshold...");
9. setThreshold(240, 255);
10. //setThreshold(240, 255);
11. setOption("BlackBackground", false);
12. run("Convert to Mask");
13. //Opening helps to destroy vascular images by "opening" the detected
    particle inside the vessel (ie. RBC) which gets ignored in detection
14. run("Morphological Filters", "operation=Opening element=Disk
    radius=10");
15. run("Analyze Particles...", "size=200-4000 circularity=0.40-1.00 display
    exclude clear summarize add");
16. //simply paste results to spreadsheet
17. String.copyResults();
18. selectWindow("original");
19. close();
20. selectWindow("Annotated");
21. roiManager("Show All");
```

APPENDIX – 3: ORIGINAL IMAGES OF ELECTROPHORESED AGAROSE GELS

1. Whole-gel image from **Figure 6A**

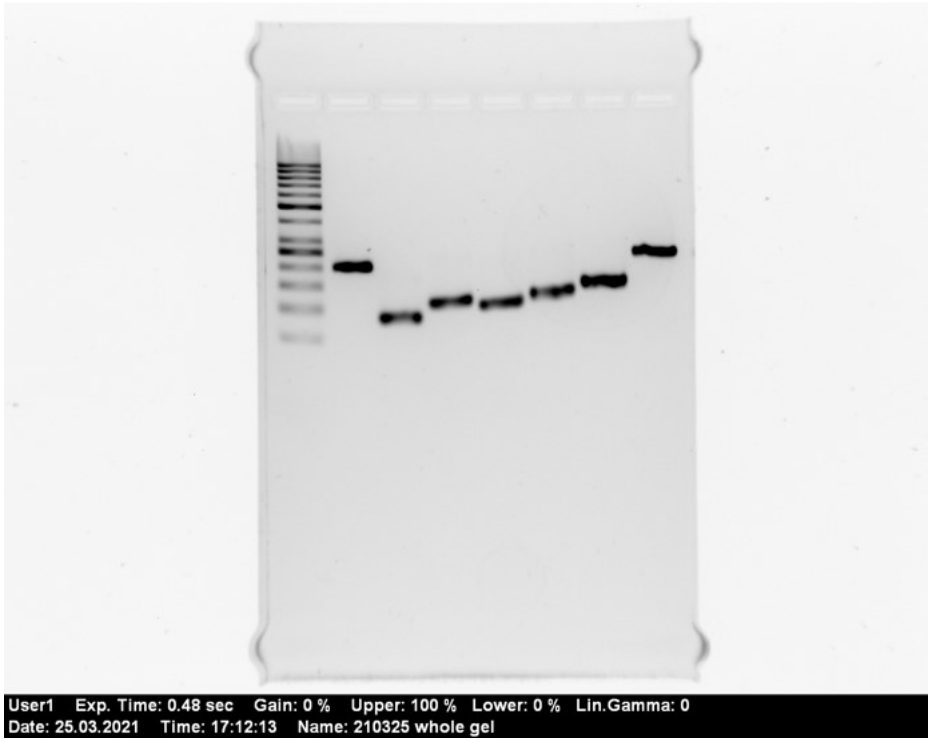

2. Whole-gel image from **Figure 6B**

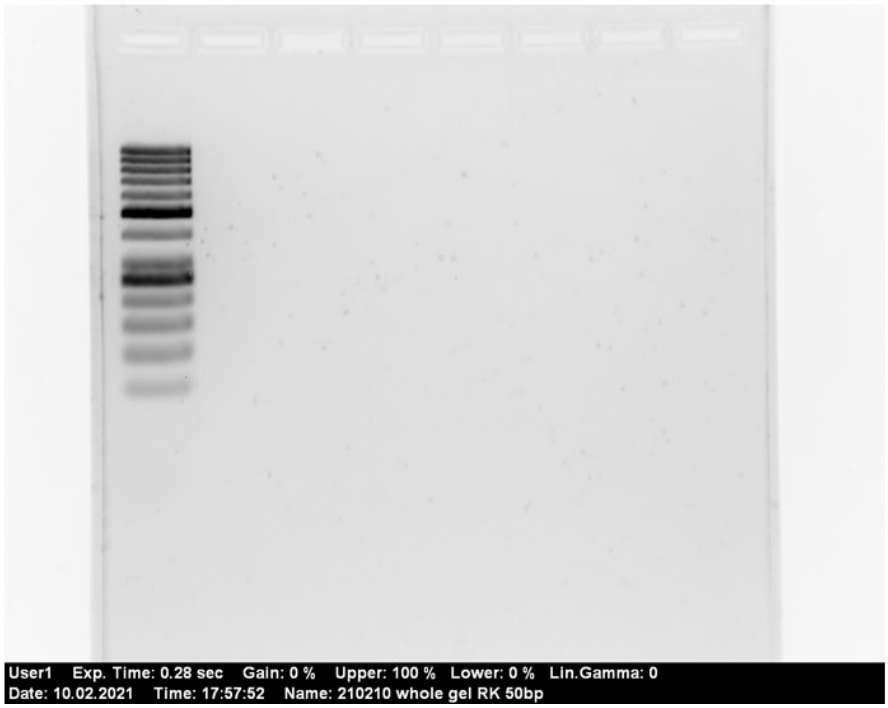

3. Whole-gel image from **Figure 9C** (upper image, UCP1 amplicons)

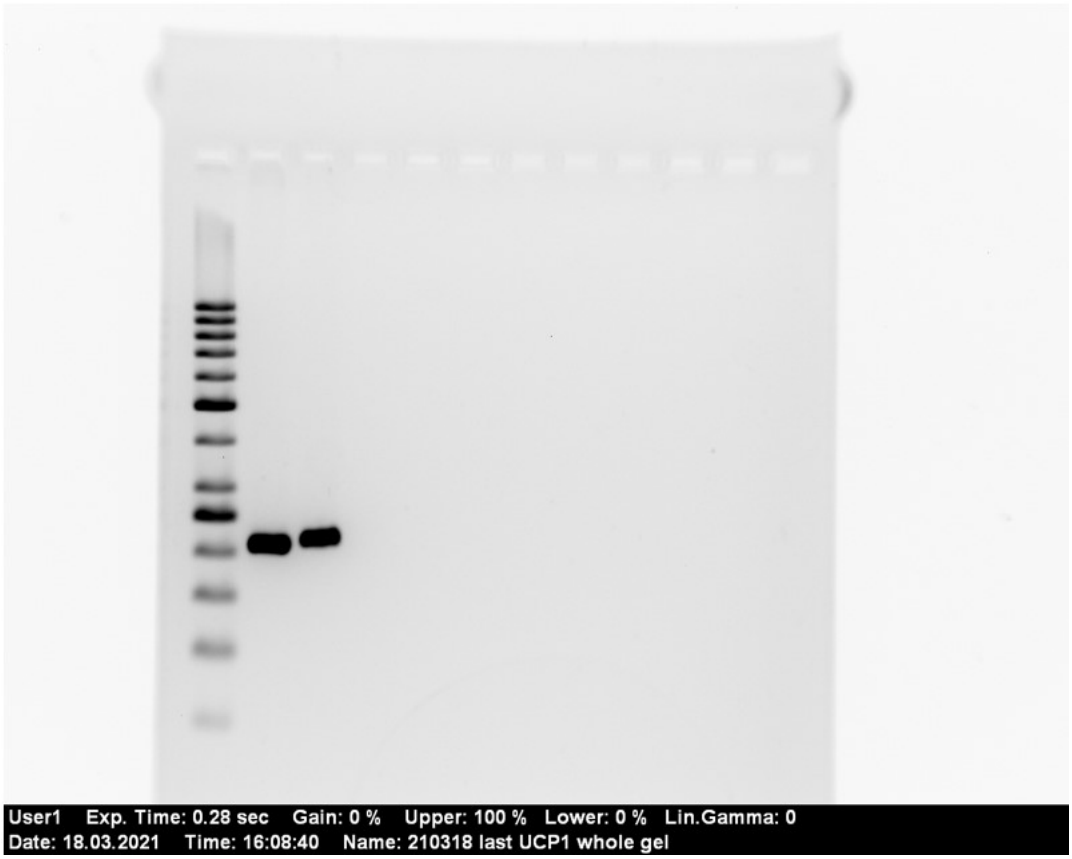

4. Whole-gel image from **Figure 9C** (lower image, CYCB amplicons)

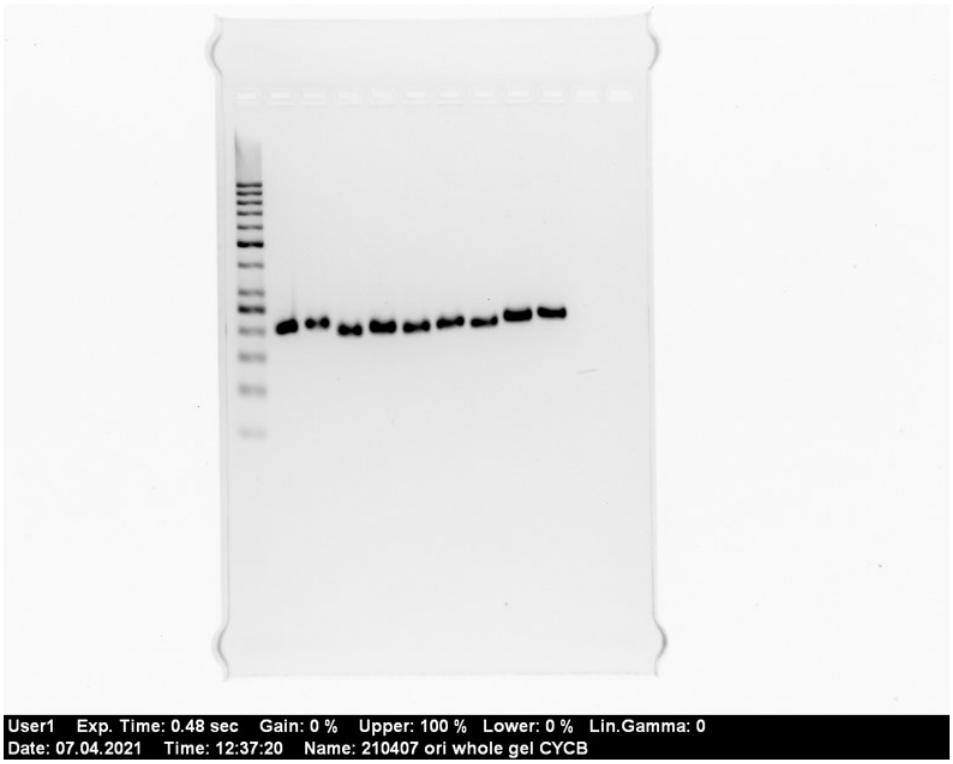

APPENDIX – 4: EXPRESSION OF BETA-ACTIN AND CYCLOPHILIN B DURING PROLIFERATION AND DIFFERENTIATION *IN VITRO*

We evaluated the mRNA expression of ACTB and CYCB from proliferating and differentiating BMSCs (two time points) based on the threshold cycle value. The results from two separate experiments were combined to assess the reproducibility. We found a significant reduction in the expression of ACTB in differentiating BMSCs *in vitro* (higher threshold cycle values) compared to the proliferating state (p= 0.01). Contrastingly, we found the mRNA expression level of CYCB to be uniform in both culture conditions.

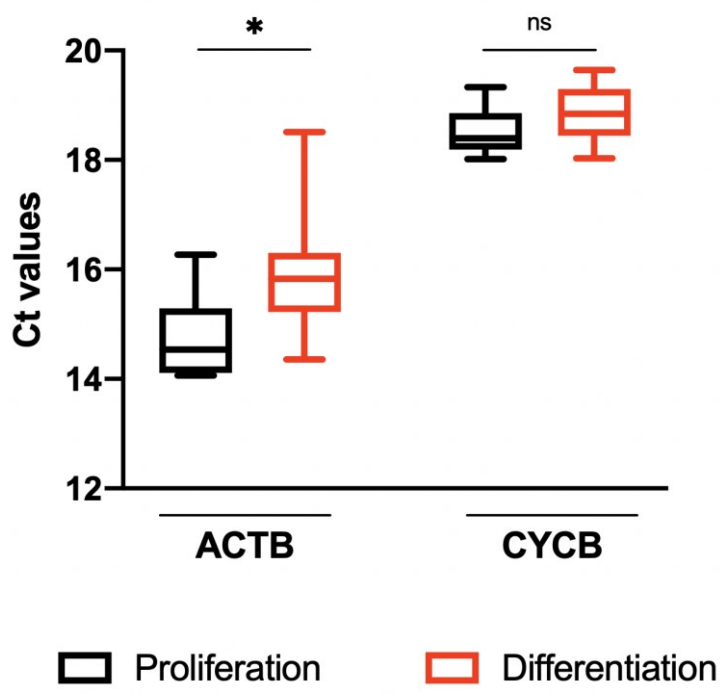

Figure S.1. Expression of the housekeeping genes ACTB and CYCB during proliferation and differentiation state of BMSCs *in vitro*. ns, non-significant.

APPENDIX – 5: EFFECT OF DMSO ON ADIPOCYTE-SPECIFIC MRNA EXPRESSION *IN VITRO*

To assess the effect of DMSO on adipogenesis *in vitro*, we induced BMSCs according to the description in **Chapter 3.1**. Briefly, BMSCs from two independent experiments (**Figure 7A and 8A**) received the adipogenic cocktail with either 0.05% DMSO (vehicle control) or none. The adipocyte-specific mRNA PPARG, ADIPOQ and FABP4 were analysed on day 6 and 12 of differentiation and compared to the respective undifferentiated control. The expression is normalised to CYCB. We noticed a transient, but significant upregulation of PPARG ($p < 0.0001$), ADIPOQ ($p = 0.003$) and FABP4 ($p = 0.001$), compared to the negative control (DMSO- group). By day 12, the mRNA expression was comparable to the negative control, except for PPARG expression ($p = 0.02$).

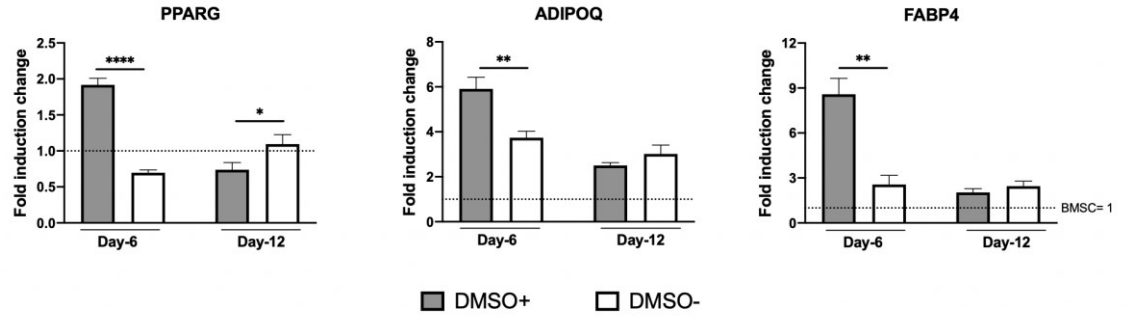

Figure S.2. Transient upregulation of the adipocyte-specific mRNA expression *in vitro* in the presence of DMSO.